Semi-automated Generation of High-accuracy Digital Terrain Models along Roads Using Mobile Laser Scanning Data

by

Lanying Wang

A thesis
presented to the University of Waterloo
in fulfillment of the
thesis requirement for the degree of
Master of Science
in
Geography

Waterloo, Ontario, Canada, 2016

AUTHOR'S DECLARATION

I hereby declare that I am the sole author of this thesis. This is a true copy of the thesis, including any required final revisions, as accepted by my examiners.

I understand that my thesis may be made electronically available to the public.

Abstract

Transportation agencies in many countries require high-accuracy (2-20 cm) digital terrain models (DTMs) along roads for various transportation related applications. Compared to traditional ground surveys and aerial photogrammetry, mobile laser scanning (MLS) has great potential for rapid acquisition of high-density and high-accuracy three-dimensional (3D) point clouds covering roadways. Such MLS point clouds can be used to generate high-accuracy DTMs in a cost-effective fashion. However, the large-volume, mixed-density and irregular-distribution of MLS points, as well as the complexity of the roadway environment, make DTM generation a very challenging task. In addition, most available software packages were originally developed for handling airborne laser scanning (ALS) point clouds, which cannot be directly used to process MLS point clouds. Therefore, methods and software tools to automatically generate DTMs along roads are urgently needed for transportation users.

This thesis presents an applicable workflow to generate DTM from MLS point clouds. The entire strategy of DTM generation was divided into two main parts: removing non-ground points and interpolating ground points into gridded DTMs. First, a voxel-based upward growing algorithm was developed to effectively and accurately remove non-ground points. Then through a comparative study on four interpolation algorithms, namely Inverse Distance Weighted (IDW), Nearest Neighbour, Linear, and Natural Neighbours interpolation algorithms, the IDW interpolation algorithm was finally used to generate gridded DTMs due to its higher accuracy and higher computational efficiency.

The obtained results demonstrated that the voxel-based upward growing algorithm is

suitable for areas without steep terrain features. The average overall accuracy, correctness, and completeness values of this algorithm were 0.975, 0.980, and 0.986, respectively. In some cases, the overall accuracy can exceed 0.990. The results demonstrated that the semi-automated DTM generation method developed in this thesis was able to create DTMs with a centimetre-level grid size and 10 cm vertical accuracy using the MLS point clouds.

Acknowledgements

First and foremost, I would like to express my greatest gratitude to my supervisor, Professor Dr. Jonathan Li, for providing me such valuable opportunity and keeping faith from beginning to end of my Master's study. It would be very difficult to complete this thesis without his continuous support, encouragement, positive remarks, and intellectual guidance. I feel very fortunate to have a chance to work with him in the past two and a half years. He gave me so much advice and helped me to gain more experiences for my Master's study.

I would like to thank my Master's Thesis Examining Committee, which includes Dr. Yongbo Liu at the Department of Geography, University of Guelph, Prof. Dr. Michael Chapman at the Department of Civil Engineering, Ryerson University, and Prof. Dr. Ellsworth LeDrew at the Department of Geography and Environmental Management, University of Waterloo. Their useful comments and suggestions increased the readability of this thesis and made a much better way to present my research findings.

I would like to thank Mr. Mark Tulloch, Chief Operating Officer, Tulloch Engineering for providing the RIEGL VMX-450 datasets used in this study. Special thanks go to Dr. Yongtao Yu who worked at the Fujian Key Laboratory of Sensing and Computing for Smart Cities, Xiamen University, and Dr. Haiyan Guan who was a former member of Mobile Mapping Lab, University of Waterloo. Without their insightful suggestions and intellectual supports, I would not be able to complete this thesis.

I was fortunate to go thorough of this road with many other graduate students, and

needless to say, it is a fantastic journey to share with you. Many thanks to Shiqian Wang, Wei Li, and Jingwen Huang shared their time and helping me to go through the first year in Waterloo. Sincere thanks to people working in Mobile Mapping Lab, University of Waterloo, especially to Weikai Tan, Menglan Zhou, Han Jiang, Lingfei Ma, He Zhao, and Haocheng Zhang for creating a friendly working environment, helping me to finish the field work, and digitalize terrain points from hundred billions of MLS points. Also, thanks to Mike Lackner, Remote Sensing Specialist at the MAD Centre, University of Waterloo, for helping to organize field work. Special thanks to Dr. Jianjun Wang, Dr. Zheng Ji, and Dr. Xiaoliang Zou. I also deeply appreciate the past and present members of Mobile Mapping Lab for their wonderful friendship, support and valuable discussion.

I am very thankful to my parents. I can say I owe tremendous thanks to them. They not only financially supported my decision, which directly led to this research, but also encouraged me to get through all this work and stress. I am also very thankful to my dear brothers and sisters in MCCF and my home church. Specially, thanks to Yuling Chang, Runyan Zhu, Wen Tang, Xiangyu Luo, Yikun Hao, and Aimee Tan for helping me working and proofreading on this thesis. Thanks everyone for always standing and walking with me, and praying for me. Hope we will continue walking together to follow Jesus Christ.

Finally, thanks to my dear God.

Table of Contents

List of Figures

List of Tables

List of Abbreviations and Glossary of Terms

2D	Two Dimensional
3D	Three Dimensional
ALS	Airborne Laser Scanning
CCD	Charge Coupled Device
DEM	Digital Elevation Model
DMI	Distance measurement indicator
DSM	Digital Surface Model
DTM	Digital Terrain Model
GCPs	Ground Control Points
Geo-referencing	The association of ground coordinates for objects
GIS	Geographic Information System
GNSS	Global Navigation Satellite System
GPS	Global Positioning System
IDW	Inverse Distance Weighted
IMU	Inertial Measurement Unit
InSAR	Interferometric Synthetic Aperture Radar
Intensity	Strength of reflectivity of returning signal from laser sensor, recorded as a numerical value and converted to 8-bit image
LAS	Lidar native file format
Lever-arm	A distance offset between two sensors
LiDAR	Light Detection And Ranging
MLS	Mobile Laser Scanning
MLS data	Point clouds collected by a MLS system
MTO	Ministry of Transportation Ontario
NAD83	North American Datum of 1983
NCHRP	National Cooperative Highway Research Program
Outliers	Points that do not represent any real objects and wrongly observed by sensor.
RMSE	Root Mean Square Error
RTK	Real Time Kinematic
SAR	Synthetic Aperture Radar
SOR	Statistical Outlier Removal
TIN	Triangulated Irregular Network
TLS	Terrestrial Laser Scanning
UTM	Universal Transverse Mercator

Chapter 1
Introduction

1.1 Motivations

1.1.1 Requirements of High-accuracy DTMs along Roads

A Digital Terrain Model (DTM) is a digital and mathematical representation of the virtual terrain information (Kasser and Egels, 2002). It is a type of Digital Elevation Model (DEM) which only measures the elevation of any point on ground or water surface. Terrain is a fundamental factor of earth surface modeling which can be efficiently represented by DTMs. Thus, DTMs have been widely used in many areas such as resource management, urban planning, transportation planning, earth sciences, environmental assessments, and Geographic Information System (GIS) applications (Vaze and Teng, 2007).

In transportation, a highly accurate DTM along roads can be used in various transportation applications. A high-accuracy DTM can be applied toward road design and construction, post-construction quality control, and the maintenance of roads and highways. For instance, highway design and construction normally requires 30 cm or 15 cm contour intervals (Maune, 2007). According to Berg and Ferguson (2001), the Ministry of Transportation Ontario (MTO) requires an accuracy of 9 cm and 23 cm (for 1:3000 scale) DTMs on hard-surface and soft-surface areas, respectively, when working on highway engineering projects. Fellendorf (2013) stated that a DTM with a height accuracy of 2-5 cm can compute the energy consumption and simulate traffic flow. The grid size and the accuracy of elevation of DTMs are relevant to the quality of the geometric design of roads

and highways (Fellendorf, 2013). In the United States, the Department of Transportation requires an accuracy of 21 cm (for 1:3000 scale) DTMs for hard surface (Yen et al., 2010). According to the National Cooperative Highway Research Program (NCHRP) of the United States, the suggested accuracy of DTMs is less than 5 cm at the engineering survey level such as pavement analysis and road and highway design, 5-20 cm at the general mapping level such as extraction of road features and autonomous navigation, and greater than 20 cm at the road condition assessment level (Olsen et al., 2013). For this purpose, generating high-accuracy and high-resolution DTMs along roads is necessary for transportation engineering projects.

In addition, pavement cracks and curbs along the road can be generated through high-resolution and high-accuracy DTMs. Moreover, high-accuracy DTMs can be implemented in transportation safety control. For example, roads surface water has a major impact on pavement skid resistance (Norrman et al., 2000). Road surface water depth and road surface run-off can be calculated by using highly accurate DTMs. The input data (DTM) quality and resolution significantly affect these final results (Kenward et al., 2000). Moreover, some terrain features extracted from DTMs, such as slope and aspect, can assist with stormwater management, disaster preparedness and response, and floodplain management. Stormwater management heavily relies on DTMs (Maune, 2007). Urban road waterlogging normally occurs in many cities such as Beijing, and Mumbai during rainy seasons, and it can result in human casualties and economic losses (Gupta, 2007; Liu et al., 2014). A high-accuracy and high-quality DTMs along roads is advantageous for urban planning and management regarding these types of disasters.

1.1.2 Techniques for Generating DTMs

Traditionally, cartographers manually plotted data points with the assistance of photogrammetric models after ground surveying to obtain DTMs (Gallant, 2000). It provides the most accurate DTM among other methods. This method requires more editing, which can be completed by using GIS, and they are costly and require a great effort. However, rapidly updating GIS data has become a new trend, and traditional surveying next to speeding traffic is hazardous and time consuming.

With the rapid development of GIS and remote sensing, these techniques allow a greater number of researchers to use remote-sensed imagery to generate DEMs. A variety of satellite images, which have different spatial, radiometric, spectral, and temporal resolutions, can provide elevation information for generating DTMs (Kayadibi, 2009). Using remote-sensed images to extract DTMs has become an attractive option as it is less labour intensive and less time consuming.

There are many research conducted in the past where satellite images used to generate DTMs. Satellite stereo images have been used to generate DTMs. Compared to a DTM generated from topographic contours at a scale of 1:250,000, a DTM extracted from SPOT stereo imagery had a median disagreement of 58 m, and it provides better basis for orthorectification (Zomer, 2002). Some researchers tried to use adjacent-orbit Landsat-7 ETM+ panchromatic images to obtain a DTM but a main problem to this approach arises as Landsat images are significantly affected by clouds, snow, and ice in mountains and high-latitude areas (Toutin, 2002). ASTER stereo data and Cartosat-1 stereo data can extract

highly-accurate DTMs (Toutin, 2006; Kayadibi, 2009). However, these two types of satellite images need to be integrated into ground control points (GCPs) as auxiliary data. After the emergence of sophisticated radar technology, methods such as radargrammetry and interferometry have been used to produce DTMs using radar images (Kayadibi, 2009). Generating DTMs using Interferometric Synthetic Aperture Radar (InSAR) images requires at least two complex Synthetic Aperture Radar (SAR) images that must cover the same area and be acquired from slightly different points of view (Crosetto, 2002). Unlike using Landsat's data for extracting DTMs, SAR or InSAR data can be used without considering weather conditions and day or night data acquisition. However, the data quality is not as high as using optical images at the same scale (Moreira, 1996; Kayadibi, 2009).

1.1.3 Laser Scanning Techniques for Generating DTMs

Airborne laser scanning (ALS), terrestrial laser scanning (TLS), and mobile laser scanning (MLS) data have been used to derive DTMs, which contain more details than those derived from photogrammetry, respectively (Abellan et al., 2009; Corsini et al., 2009; Lato et al., 2009). In addition to the improvement of spatial resolution, vertical accuracy can be improved as well. Compared to other methods, laser scanning data acquisition is rapid, affordable, and capable of reaching inaccessible areas (Heritage and Large, 2009). Since laser scanning data usually achieves centimetre level precision in the vertical direction, researchers recently began to focus on using laser scanning systems to obtain DTMs.

Laser sensors are equipped on different platforms, such as ground-based platforms, or moving platforms: an airplane, a vehicle, a boat, and even a human carried backpack (Kukko

et al. 2012; Williams et al., 2013). Because of this, the features of data acquired from these different methods are diverse. A typical urban road profile is shown in Figure 1.1. Traditionally, for generating topographical information, people tend to use automatic levels, total stations, or GPS. As Profile A shows, this method usually obtains less data and is time consuming. In addition, surveying in urban areas especially on roads or highways, is quite dangerous for operators.

Laser scanning data has much more topographical details which help with generating DTMs and Digital Surface Models (DSM). Compared to DTMs, DSM not only represents the elevation of any point on ground or water surface, but also contains the elevation of all features above the ground. ALS systems can collect not only the terrain features but also the objects above the ground with dense point clouds as shown in Profile B. This kind of laser scanning data usually shows a point density up to 20 points/m² (Zippelt and Czerny, 2010). However, as Profile C shows, TLS and MLS can observe and measure very high dense point clouds, usually up to several thousand points per square meter for all objects which are terrain or off-terrain points. After the raw data is processes, new details and information with finer resolution can be provided. Since then, the usage of topographic mapping as the fundamental function of MLS systems has become very prominent (Olsen et al., 2013). Lin and Hyyppa (2010) successfully proposed an automatic method for detecting pedestrian culverts from DTMs created from MLS point clouds, which helps supplement roadway characteristic attributes. Their work demonstrates that it is possible to generate DTMs along the road from MLS data. Meanwhile, the development of MLS technology advances as more advanced MLS systems that can efficiently collect data with higher positional accuracy, were

invented by manufacturers. For instance, 1.1 million points can be collected in one second by RIEGL VMX-450 system (RIEGL, 2013). Surveying a 10-kilometre highway using the traditional method usually takes over 20 nights. However, to finish all these works, the MLS system only takes less than one week (Olsen et al., 2013). Most MLS systems can provide an absolute accuracy less than 5 cm. Therefore, generating high-accuracy and high-quality DTMs along roads can be achieved. Compared to other methods, MLS systems provide a labour-effective method to acquire high precision topographical information.

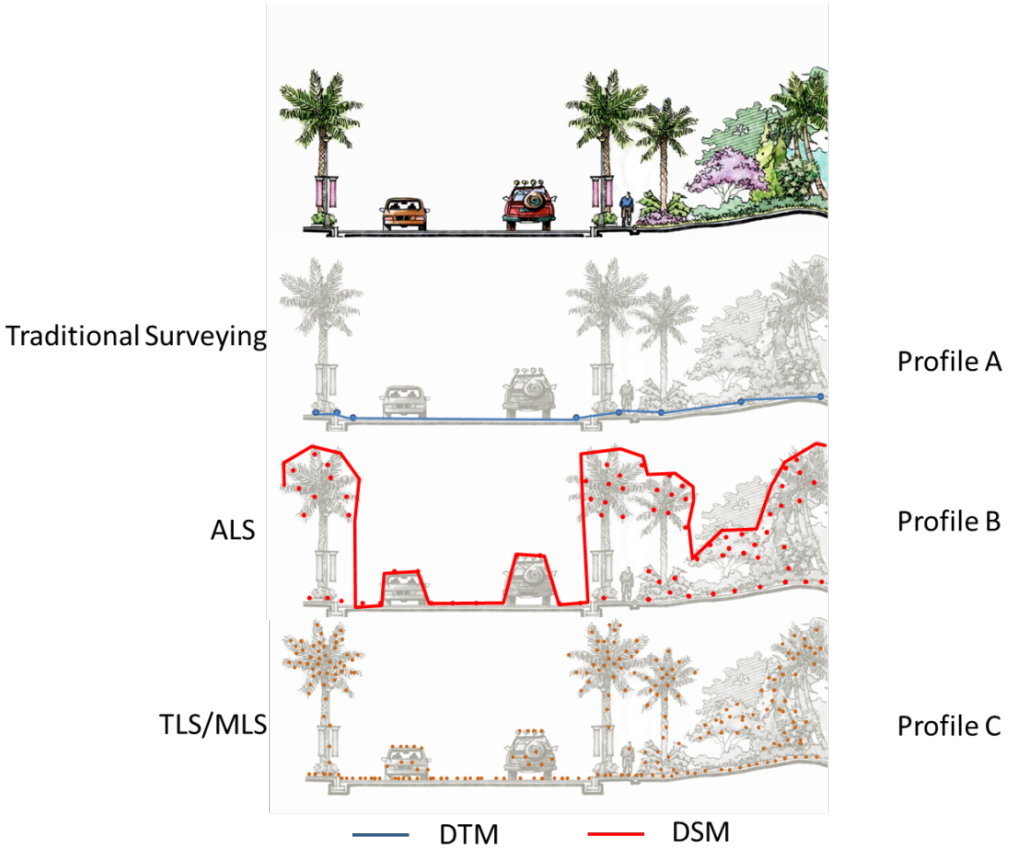

Figure 1.1: Example of traditional surveying and different laser scanning observations.

1.1.4 Challenges in DTM Generation by MLS Data

To generate a DTM from MLS data, data processing could be a challenge. Data post-processing has been identified as a new challenge to the industries since MLS data sets usually have huge volumes. As a result, data processing capability is significant to the efficiency and accuracy of the final deliverable topographical information, such as DTMs. There have been several commercial software packages available such as TerraSolid software, Leica Cyclone®, InnovMetric PolyWorks®, GeoCue software suite, PHOCAD PHIDIAS®, Bentley Pointools, and Virtual Geomatics software suite (Yen et al., 2011). However, many of these packages were originally developed for ALS data processing. For example, the Terrasolid® software suite can only process point clouds with dozens of megabytes in each data strip. MLS data commonly holds hundreds of megabytes in each data strip. In addition, some manufactures developed packages to process MLS data such as RIEGL's Ri-SCAN PRO and Ri-PROCESS (Guan, 2013). But these software packages only provide some fundamental functions when processing MLS data, including data control, calibration, adjustment, registration, and visualization, rather than processing data further for the purpose of delivering more detailed geographical products such as DTMs (Guan, 2013).

In addition, several MLS-based studies have been conducted by our research group, including the development of algorithms and software tools for automated detection and extraction of 3D off-terrain objects (e.g., vehicles, traffic signs, and street light poles), and road information (e.g., road markings, pavement cracks, and manhole covers) (Guan et al., 2015a; Guan et al., 2015b; Wen et al., 2015; Yu et al., 2015a; Yu et al., 2015b). However, there is no research working on using MLS data to generate DTMs along roads. Therefore,

this thesis attempts to address the following three key research questions:

(1) How efficient is DTMs generation from MLS data?

(2) How good of DTMs generated from MLS point clouds can be achieved in terms of accuracy and resolution?

(3) How different densities of MLS point clouds effect the accuracy and resolution of DTMs?

1.2 Objectives of the Study

The main research goal of this study is to develop a method for automatically generating high-accuracy DTMs using MLS data. More specifically, the objectives of this study are summarized as follows:

- To develop a semi-automated filtering algorithm to extract terrain points from raw MLS point clouds;
- To generate centimetre-accuracy gridded DTMs based on the high-density terrain points segmented from the MLS point clouds using a simple and efficient interpolation method;
- To assess the quality and accuracy of the proposed filtering approach and the derived DTMs using the MLS data acquired in the selected study area.

1.3 Structure of the Thesis

This thesis consists of five chapters. Chapter One provides the motivations and

objectives of this study. Chapter Two reviews the elements of a typical MLS system and various previous studies on the generation of DTMs using ALS, TLS and MLS point cloud data. Chapter Three presents the study area, analyzes the collected MLS data, and explains the designed method of filtering ground points from MLS data and generating DTMs from ground points. Meanwhile, how to assess the accuracy of proposed approach is described. Chapter Four details and compares the results, which obtained from the filtering algorithms, and quantitatively and qualitatively analyzes the filtering performance. In the meantime, gridded DTMs generated by several interpolation methods are analyzed and discussed through internal and external accuracy assessments. Chapter Five concludes this research with contributions of the study, limitations, and outline direction for future research.

Chapter 2
Background and Related Work

This chapter presents the literature review which related to this research. Section 2.1 describes the principle of mobile laser scanning. Sections 2.2 and 2.3 provide the literature review of existing algorithms that have been used for ground filtering and some critical issues in those algorithms. Section 2.4 reviews some existing methods for interpolating discrete points into continuous surface as DTMs. Section 2.5 summarizes this chapter.

2.1 Principle of Mobile Laser Scanning

2.1.1 Components of a Mobile Laser Scanning System

In general, a typical MLS system consists of five essential parts: (1) a mobile platform, (2) a navigation solution system which integrates a Global Navigation Satellite System (GNSS), an Inertial Measurement Unit (IMU), and a wheel-mounted Distance Measurement Indicator (DMI), (3) laser scanner(s), (4) digital camera(s), and (5) a control system (Puente et al., 2013).

(1) A mobile platform

The platform carries all data collection hardware into one system. This platform can be a vehicle used in this thesis, or a boat, a train, or a stroller.

(2) A navigation solution system

A navigation solution system of a MLS system is composed of a GNSS, an IMU, and a wheel-mounted DMI. GNSS antenna monitors three primary measurements including time,

position, and velocity (speed and direction) (Glennie, 2007). Even a GNSS sensor can acquire high-accuracy positional information in most areas; it is still affected by high-rise buildings, high trees, and other barriers that may block satellite signals (Glennie, 2007). At the same time, the IMU observes the posture information including roll, pitch, and heading of the vehicle. It provides both accelerations and angular rotations in three coordinate axes. In addition, IMU can work without satellite signals. Thus, IMUs can continually fill the gaps between the former and later GNSS observations which update the GNSS positions in periods of poor satellite signal conditions (Williams et al., 2013).

Reciprocally, the GNSS helps to updating positioning information to IMU. DMI is equipped on one of the vehicle wheels, and measures the tire rotation to calculate a travelled distance of the vehicle (Glennie, 2007). DMI provides supplementary positioning information for the GNSS and IMU.

(3) Laser scanner(s)

In different MLS systems, the number and the type of scanners may vary. Continuous waves or pulses are emitted from laser scanners to scan objects (Glennie, 2007). Recently, there are two main ranges measurement methods of laser sensors: time-of-flight and phase shift (Lichti, 2010). The difference between these two types sensors is the time-of-flight method uses the time difference, while the phase shift method is more accurate based on the phase differences (Petrie and Toth, 2008; Beraldin et al., 2010). In terms of scanning head, there are two kinds of laser scanners: fixed scanning head laser scanner and rotated scanning head laser scanner. The quality of a laser scanner is determined by the level of eye safety, the

data accuracy, the field-of-view, the data resolution, and the scan rate (Guan, 2013). Some scanners can also keep the intensity values which are the strength value of return signals that helps distinguishing the different reflectance from targets (Williams et al., 2013). Most laser sensors use the eye-safe near infrared laser light which the electromagnetic spectrum range is at 1040 to 1060 nm, and the measurement frequencies are always up to 200,000 points per second (Optech, 2009). The operating principle of a laser scanner is measures the round-way travel time of one laser pulse traveled to the object.

$$d = c \times \frac{t}{2} \tag{2.1}$$

where d is the distance between the laser scanner and the object, t is the travel time, and c is the known the speed of light in vacuum (299,792,458 ms^{-1}).

(4) Digital camera(s)

In addition, ancillary data such as photos and/or videos taken via digital camera can also contribute to survey by MLS system. For example, in terms of visualization, MLS Data cannot provide the true-colour information in reality. However, after integrating records of digital cameras, people can acquire more detailed data in color and features (Guan, 2013; Williams et al., 2013). Similarly, the number and types of the camera depend on different MLS systems.

(5) A control system

A control system is a type of computer system that integrates the navigation system,

laser scanner(s), and camera(s) working well but it requires storing a large quantity of data.

2.1.2 Direct Geo-referencing and Error Analysis

As an active remote sensing technique, LiDAR can directly and efficiently provide 3D coordinates (x, y, z) point clouds in both horizontal and vertical directions. From the point clouds, the geographical coordinator of every object on the ground surface can be acquired such as trees, buildings, power lines, terrain, and other above-ground objects.

In a MLS system, a GPS and an IMU are quite important to determine the position and orientation of the system. Because they provide a reference to a mapping coordinate system for each laser measurement (Barber et al., 2008). In other words, the quality of MLS data depends on laser sensors and the whole integrated navigation solution system (including GPS, IMU, and DMI). In order to have the exact coordinates of mapping points, observations in the ground coordinate are calculated by Equations 2.2 and 2.3 through time-stamped navigation data (Glennie, 2007; Barber et al., 2008). The coordinates of a target P shown in Figure 2.1 can be calculated by:

$$\begin{bmatrix} X_P \\ Y_P \\ Z_P \end{bmatrix}^M = \begin{bmatrix} X_{GPS} \\ Y_{GPS} \\ Z_{GPS} \end{bmatrix}^M + R_{IMU}^M(\omega, \varphi, \kappa) \cdot \left(R_S^{IMU}(\Delta\omega, \Delta\varphi, \Delta\kappa) \cdot r_P^S(\alpha\ d) + \begin{bmatrix} l_X \\ l_Y \\ l_Z \end{bmatrix}_S^{IMU} - \begin{bmatrix} L_X \\ L_Y \\ L_Z \end{bmatrix}_{GPS}^{IMU} \right) \quad (2.2)$$

$$r_P^S(\alpha\ d) = d_P^S \cdot \begin{bmatrix} \cos\alpha \\ 0 \\ \sin\alpha \end{bmatrix} \quad (2.3)$$

where,

X_P, Y_P, Z_P are the location of the target P in the mapping frame.

$X_{GPS}, Y_{GPS}, Z_{GPS}$ are the location of GPS antenna in the mapping frame.

$R_{IMU}^{M}(\omega, \varphi, \kappa)$ is the rotation matrix between IMU and mapping frame, (ω, φ, κ) are the roll, pitch and heading of the sensor with respect to the local mapping frame. These values are provided by the IMU system.

$R_{S}^{IMU}(\Delta\omega, \Delta\varphi, \Delta\kappa)$ is the rotation matrix between the laser scanner and IMU, $(\Delta\omega, \Delta\varphi, \Delta\kappa)$ are the boresight angles which align the scanner frame with IMU body frame. Those values are determined by the system calibration.

$r_{P}^{S}(\alpha\ d)$ is the relative position vector of Point P in the laser scanner coordinate system. α and d are scan angle and range measured and returned by the laser scanner, respectively.

d_{P}^{S} is the range from laser scanner to the observed object.

$l_X,\ l_Y, l_Z$ are lever-arm offsets from the navigation and IMU origin to the laser scanner origin. These values are determined by system calibration or measurement.

L_X, L_Y, L_Z are lever-arm offsets from the IMU origin to the GPS origin. These values are determined by system calibration or measurement.

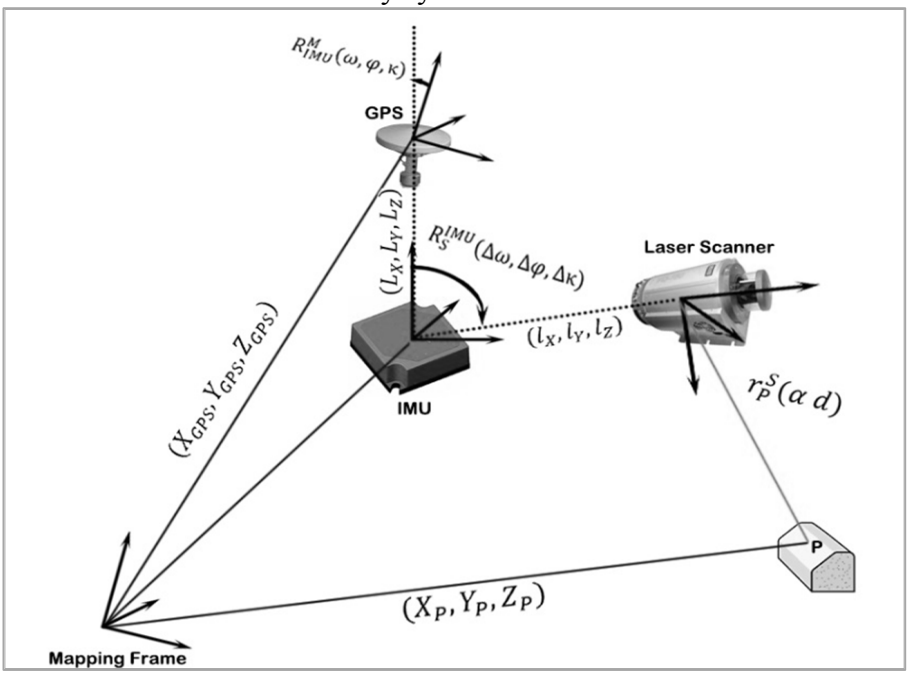

Figure 2.1: Principle of direct geo-referencing.

Equations 2.2 and 2.3 explain the relationship between the geo-referenced MLS data and the measurements of observed targets, which determines the accuracy of the final point cloud. Therefore, some typical errors can be pre-analyzed through these parameters (Glennie, 2007).

(1) Positioning errors: Since a number of factors, such as multipath, atmospheric errors, baseline length, poor satellite geometry, and loss of lock can directly affect the results of the observation; the absolute level of positioning accuracy for the GPS system is difficult to quantify (Glennie, 2007). In ideal conditions, the accuracy of positional data is expected as 2cm +1 ppm horizontally and 2cm +1 ppm vertically within a relatively short kinematic baseline (< 30 km) (Glennie, 2007).

(2) IMU attitude errors: The Inertial Measurement Unit measures roll, pitch, and yaw angles which equate the rotation from the IMU into the mapping frame. An IMU constantly provides the acceleration along a specific axis and measures and maintains orientation of the MLS system frame (Glennie, 2007). Thus, system errors of IMU sensor include accelerometer biases and gyro drifts (Guan, 2013).

(3) Laser scanner errors: Typically, system errors of a laser scanner have two main parts: errors in distance and errors in angles. Distance errors are usually caused by the accuracy of internal time measures including the time of flight and the width of the output laser pulse (Glennie, 2007). The errors in angle depend on the angular resolution of the angle encoder of laser sensor and the deviation of beam

divergence.

(4) Boresight errors: Misalignments of axes between IMU and laser scanner measurement cause boresight errors. In order to acquire high-accuracy laser scanning data, the location and orientation of the laser scanner relevant to the IMU must be precisely known. An alignment error can affect the distance between the laser and the scanned object. According to Rieger et al. (2010) and Lim et al. (2013), boresighting should be an extremely precise measurement process which pursues any mounting misalignment correction between the IMU and laser scanner.

(5) Lever-arm offset errors: To obtain high-quality georeferenced MLS points, the lever-arm offsets must be known. However, the origins of laser sensors and IMU usually cannot be co-located (Barber et al., 2008). Therefore, calibration and physical measurement are two approaches to access the lever-arm offsets. Physical measurement is widely used since it is easy to apply, but the measurement error is another problem because of the uncertainty to align axes of laser scanner and IMU (Guan, 2013).

According to these error sources, the accuracy of MLS data is highly depends on the accuracy of navigation solution system and laser scanners, because both boresight and lever-arm errors can be corrected by system calibration (Guan, 2013). Secondly, GPS system conditions on a moving vehicle are very critical because high-rise buildings and trees along the street may cause multi-path effects and signal shading (Barber et al., 2008; Haala et al.,

2008). Thus, the accuracy of MLS data mainly depends on the navigation solution system.

2.2 Ground Filtering Techniques

Researchers have developed a wide range of filtering algorithms to separate terrain points (ground points) from off-terrain points (non-ground points) using laser scanning data (Sithole and Vosselman, 2004; Meng et al., 2010). Several important things that should be considered when separating terrain points from off-terrain points, including types of input data, iterative characteristics, penetration of laser scanning, pre-processing steps, neighbourhood types, and other key factors used in the filtering process.

The basic idea of a slope-based filter is using the slope or difference in elevation between two points to perform a filtering operation locally. There will be some misclassifications if the off-terrain object matches the criteria on slope and elevation difference (Vosselman, 2000; Roggero, 2001; Sithole, 2001; Vosselman et al., 2001). This means that a digital surface model (DSM) is created from all first-return points. Then, the next step is to generate a slope map from the DSM and remove all slope areas above the identified threshold. Then, evaluate the removed area: if the deleted areas are not right, repeat the former step until all data are correct; if the deleted areas are right, apply the focal majority filter and focal mean filter in order which can fill the leftover areas and deleted areas.

Morphological filters provide a quantitative description of a geometrical structure (Kilian, 1996; Wack and Wimmer, 2002; Zhang et al., 2003). Thus, it is necessary to resample irregularly original point clouds into a raster before operation. Although

morphological methods are conceptually simple and can be easily implemented, rasterization of point clouds, in addition to resulting in a loss in precision, has to interpolate raster heights in some areas without points (Pfeifer and Mandlburger, 2008).

Axelsson (2000) stated using progressive triangulated irregular network (TIN) densification to filter the Lidar point clouds. This filter has been used in the commercial software Terrasolid®, which is well known for robust and steady for modeling discontinuity surfaces especially in urban areas (Guan et al., 2013). The main assumption in this algorithm is that all objects on the ground are usually higher than on-ground points. The first step is calculating initial parameters and choosing seed points which are the lowest point in a defined size (largest object size) grid. At the same time, some seed points will be removed to minimize grid size by fitting the median value which estimated from the histograms. Then, using all seed points extract a TIN as an initial DEM. Lastly, all points will be iterated, and once they match the TIN facet they will be classified in to on-ground class. In the iterative process, which the TIN and the thresholds are recomputed, the process will repeat until no more points meet the threshold values (Axelsson, 2000). Von Hansen and Vogtle proposed a similar method with some differences: the seed points were the lower part of the convex hull of the point sets, and the offset of vertical distance was used into analysis (Riaño et al., 2004). Sohn and Dowman (2002) described a reversed method which applied the progressive densification first. All these proposed filters used triangulation to access the point clouds data.

Surface-based algorithms start with the assumption that the terrain is a continuous or piecewise continuous surface. In this case, the concept of the filter is to select the lowest

point in each user-defined cell from all points, and these points will serve as the robust interpolation for the initial parametric surface. The robust interpolation's general principle, such as linear least squares interpolation and Kriging interpolation, is using locally weighted regression to classify the points into on-ground and non-ground classes. Then new points are added only if they meet certain data-derived threshold parameters (e.g., difference in elevation, slope) (Kraus and Pfeifer, 1998; Axelsson, 2000; Sohn and Dowman, 2002; Krzystek, 2003; Nurunnabi et al., 2013). Pfeifer et al. (2001) stated a hierarchical-based robust interpolation method to deal with larger size buildings and reduce computational time. In Elmqvist (2001), the iteration begins with a horizontal surface below all points and moves upwards to reach the points following the negative gravity, and uses inner stiffness to classify points on vegetation or roofs.

Some cases focus on a set of segmentation-based and clustering methods, which are popular techniques in land-use and land-cover classification; these methods are used in classifying on-ground and off-ground Lidar points (Akel and Zilberstein, 2004; Akel et al., 2005; Sithole and Vosselman, 2005; Tovari and Pfeifer, 2005; Filin and Pfeifer, 2006; Pfeifer and Briese, 2007). Segmentation methods focus on rasterized point clouds instead of dealing with individual point which are less affected by noise (Pfeifer and Mandlburger, 2008). Most studies have good results in carrying out on relatively flat ground surfaces.

In addition, many researches focused on filtering road surface points from MLS data. Takashi and Kiyokazu (2006) extracted road lanes with curvature, yaw angles, and offsets information from point clouds by Hough Transform. Yuan et al. (2010) proposed a fuzzy

cluster method based on segment points and a weighted least-square linear fitting algorithm to detect the road points. But these computational methods of road points' detection are time consuming. Smadja et al. (2010), Yang et al. (2013), and Guan (2013) presented a method to filter road points based on curb candidates along the road to detect the road points. However, these methods need extra ancillary information such as multi-frame accumulated map, and trajectory of measured points. All these methods only focus on the point on road surface detection; thus, those points beside the road surface become useless since they also contain the same information as road surface.

2.3 Critical Issues in Ground Filtering

Most of these filtering algorithms have a poor performance when applying terrain surfaces with complex features such as steep slopes, large building structures or breaklines. Specifically, steep slope areas are covered by dense vegetation or artificial structures, as well as features of landform changes, are difficult to extract its DTMs because of fewer Lidar points reflecting by the ground surface or large height differences at small horizontal distances (Kobler et al., 2007). Hyppä et al. (2000) evaluated and discussed that the vertical accuracy of DTMs generating by laser scanning data of forested areas is related to terrain slop, point density and vegetation types. Liu (2008) stated that it is difficult to automatically filter on-ground and off-ground points from laser scanning points especially for large areas with various terrain characteristics.

Sithole and Vosselman (2004) indicated that some situations may lead to most algorithms failing in terrain points filtering. First, low outliers usually come from multiple

sources errors in a MLS system, while many algorithms are based on the assumption that the lowest points belong to the on-ground point class. This may cause an erosion of neighbour points of the low outlier. Second, the complex objects pose another problem in the filtering process. Some methods require a user-defined grid size for computing; although they meet the over-size objects, the on-ground points would be misclassified. For example, if the size of buildings is larger than the defined thresholds, then these buildings cannot be completely removed from the DSM. Similarly, when dealing with urban area data, vehicles are hard to remove due to their overall small size. Furthermore, some irregular shapes objects, such as low walls and irregular shape building, can cause the filter failure. Third, if roofs of building on a steep slope are as high as their surrounding surfaces of terrain, then it would be difficult to remove them from Lidar data. For instance, San Francisco, as a coastal city in the USA, has a complex terrain situation. In this case, the building on the hills will directly affect the final DTM accuracy when using some of these algorithms. Last, many filtering that are based on above terrain objects are discontinued with the terrain. Therefore, some discontinued terrain features like breaklines will influence the final DTM accuracy.

As most filtering have their unique assumptions, the filtering algorithm should focus on a certain terrain type like an urban area or a forest area to improve the accuracy of DTM generation. Moreover, most of these filters were originally designed for ALS point clouds. Some available commercial software usually has limitations on number of points. For instance, ArcMap only can handle no more than 5 million points and TerraSolid works with tens million points (TerraSolid, 2014; ArcGIS, 2015). However, MLS data usually has much higher number of points and density of points. The computational time of applying these

filters is lengthy when processing high density points or high volume point clouds.

2.4 Interpolating DTMs from Ground Points

DTMs can be stored in GIS databases in several data structures: set of contours (vector format), regular grids (raster format), and TIN (vector format). Compared to contour and TIN, gridded DTMs have good performance on surface analysis and storage simply (Weibel and Heller, 1993). Since gridded DTMs are simply represented by elevation matrices, which storage topographical relations between grids, raster format DTMs has been the most wildly used data structure to represent DTMs (Wilson and Gallant, 2000).

After obtaining all on-ground points, generate a gridded DTM requires interpolation to be the next step. Choosing an appropriate interpolation method is very important because after applying different methods the results could be totally different even using the same data source (Arun, 2013). There are several interpolation methods which can be divided into two groups: global and local methods. Global interpolation methods compute all available data points in the region of interpolation to acquire the estimation and capture a general trend of terrain relief (Wilson and Gallant, 2000; Li and Heap, 2014). For example, thin plate splines, trend surface analysis, regression models, and classification interpolation are global interpolation (Li and Heap, 2014). Since the Lidar data sets always in huge volume, the global interpolate algorithms are impracticable in computation (Wilson and Gallant, 2000; Shan and Toth, 2008). Therefore, they cannot be easily used into a real terrain surface DEM generation especially in laser scanning data.

Local interpolate algorithms, such as Inverse Distance Weighted (IDW), Kriging,

Nearest Neighbour, and triangulation, achieve better efficiency than global interpolations (Wilson and Gallant, 2000). Local interpolation methods apply within a pre-defined small area around the point being predicted and capture the local difference (Burrough and McDonnell, 1998). The local interpolation methods calculate the unknown point's value based on the values of neighbourhood points. Table 2.1 describes some widely used local spatial interpolation methods which can be applied into gridded DTMs generation (Li and Heap, 2014).

Nearest Neighbour interpolation searches the closest user-defined subset of all data to a target point and gives weights to target points by proportion of areas (Sibson, 1981). Considering the exactness of interpolation methods, nearest neighbour interpolation assigns estimated value exactly the same as value at a sampled point (Burrough and McDonnell, 1998). The drawback of Nearest Neighbour interpolation is that it only processes one nearest reference point into the final interpolating.

Triangulate interpolation constructs triangles which can be 2D or 3D through the data points, and then a local polynomial function will be applied across every triangle in TIN (Wilson and Gallant, 2000). The advantage of triangulate interpolation is that even when the real terrain surface has various structures such as breaklines this method can still work well due to its strong adaptability (McCullagh, 1988). Nonetheless, triangulation methods are limited by their sensitivity to the points' position, making them difficult to interpolate contour data (Clarke, 1990).

Table 2.1: Comparison of available local spatial interpolation methods.

Method	Assumption	Exactness	Limitation of the Procedure	Computing Load	Suitability
Nearest Neighbour	The best local predictor is the nearest neighbour data point.	Exact	No error assessment and only one data point per pixel is used	Small	Nominal data from all known points
Triangulation (TIN)	The best local predictor is data points on the surrounding triangle.	Exact	No error assessment and TIN pattern relays on distribution of data	Small	Quick interpolation on regularly or irregularly spaced data
Natural Neighbours	The best local predictor is data points on the surrounding Voronoi polygons.	Exact	No error assessment	Small	Quick interpolation on regularly or irregularly spaced data
Inverse Distance Weighting (IDW)	The underlying surface is smooth.	Inexact (but can be forced to be exact)	No error assessment and the result depend on weighting parameter	Small	Quick interpolation on regularly or irregularly spaced data
Local trend surfaces	The best local predictor is the nearest neighbour data point and data normality.	Inexact	The final result depends on span parameter and detail of the known data surface	Moderate	Quick interpolation on regularly or irregularly spaced data
Kriging	The interpolated surface is smooth and statistical stationary and the intrinsic hypothesis.	Exact	Error assessment depends on variogram and distribution of reference points and the size of interpolated grid	Moderate	Provides a good interpolator for sparse data when data are sufficient to compute variogram

According to Webster and Oliver (2001), Natural Neighbours has better performance than Nearest Neighbour and TIN since it estimated a continuous and smooth surface. It can also quickly interpolate on regularly or irregularly spaced data. The IDW is a local deterministic interpolation that predicts the value using "a distance-weighted average of sampled points in a defined neighbourhood" (Burrough and McDonnell, 1998). This means the closer between reference points and the target point, the higher weighted of the sample points with inverse of their distance to the target point. IDW predicted values of estimated point different from those reference values, but IDW can make the predicted value to be the same as the known point (Li and Heap, 2014).

Local trend surfaces predict an inexact value based on the assumption that best local predictor is the nearest neighbour data point and data normality. This method provides gradual surface but the computing load is higher than other method (Webster and Oliver, 2001). Kriging interpolation is a geo-statistical-based interpolation method, and it is more related with the spatial relationship of data rather than their values. If the variogram models been used are good enough, a high quality result can be generated (Li and Heap, 2014).

2.5 Chapter Summary

This chapter first reviewed detailed background knowledge of MLS technology, including a description of main components of a typical MLS system, the principle of how to geo-reference raw laser pulses into a map projection, and analysis some potential errors of MLS data. In addition, variety filtering terrain point's methods for laser scanning data were reviewed. Some critical issues of DTM generation process were presented. Most of these

filtering method were originally developed for ALS data, which are quite time consuming when uses them for MLS data. Some of existing methods cannot process MLS point clouds that contain steep slopes, different sizes buildings, and irregular-shape objects above the ground. Lastly, current available spatial interpolation methods for DTM generation were also introduced and analyzed. The local interpolation methods are more suitable in this study.

Chapter 3
Methodology

This chapter presents the methodology of this research. Section 3.1 describes the workflow of generating DTMs along road from MLS point clouds. Sections 3.2 and 3.3 detail the study area and dataset used in this study, and a pre-processing procedure. Section 3.4 introduces the concept of proposed terrain point filtering algorithm. Section 3.5 describes interpolation methods that will be used in ground point interpolation. The accuracy assessment methods are described in Section 3.6.

3.1 Workflow

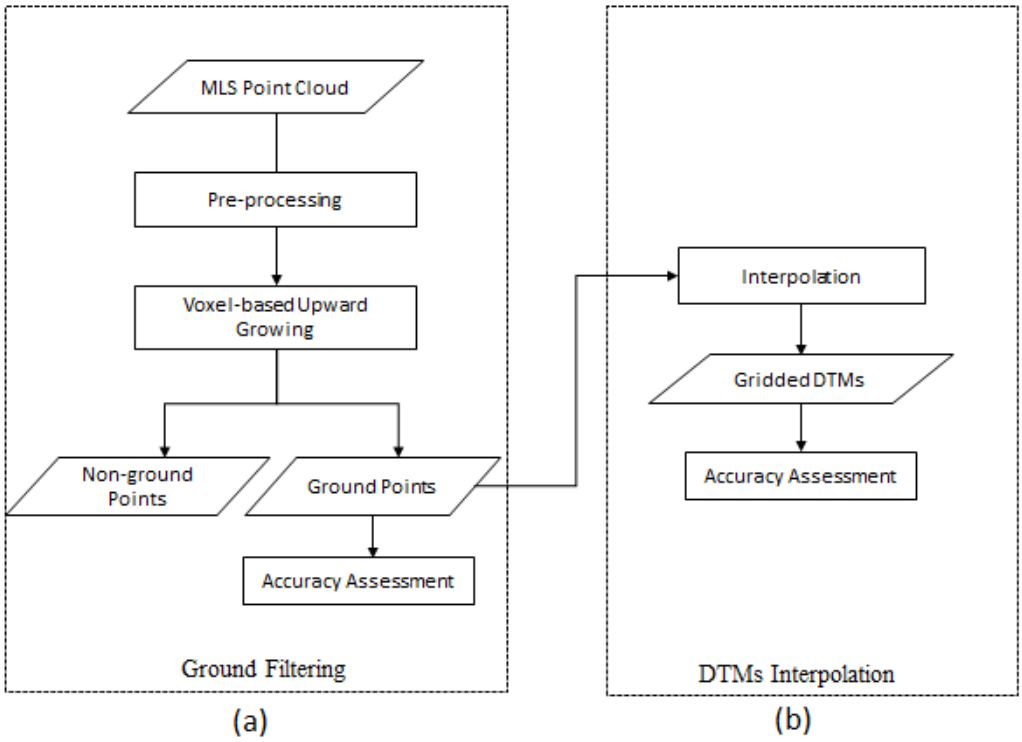

Figure 3.1: Workflow of ground filtering and generating DTMs from mobile laser scanning point clouds.

Figure 3.1 presents the workflow with five processes. Firstly, the MLS datasets are pre-processed to remove lower outliers. Then ground points are retrieved by filtering. After filtering, ground points are interpolated into gridded DTMs after evaluating filtering results. Finally, the accuracy of gridded DTMs is assessed. These processes will be detailed in the following sections.

3.2 Study Area and Datasets

3.2.1 Study Area and MLS Dataset

The surveyed area is within Kingston, Ontario, Canada (longitude 76°33'22.57"W, latitude 44°13'7.40"N). As shown in Figure 3.2 (a), Kingston is a city located in Eastern Ontario where the St. Lawrence River flows out of Lake Ontario. It is in the midway between Toronto and Montreal. As shown in Figure 3.2 (b), this surveyed road is a part of King Street West and Front Road. The west part of this surveyed road is nearby the lakeshore of the Lake Ontario. The total distance of the surveyed road was around 3.7 km. It mainly is a two-direction, four-lane road, and some parts of the road are two-direction, two-lane road. There are a few tall buildings, many houses, tall trees, grasslands, and other objects (e.g., light poles, traffic poles, power lines and poles) are along the road. Some surveyed data includes point clouds of pedestrians, vehicles and trains.

This dataset includes the trajectory, point clouds LAS files, and digital images. The data were acquired on 29 August 2013 by a RIEGL VMX-450 system from Tulloch Engineering. This system comprises two RIEGL VQ-450 laser scanners, four CS-6 CCD cameras, and a set of Applanix POS LV 520 processing system containing a GPS, an IMU,

and a DMI (see Figure 3.3). As depicted in Figure 3.4 (a), the RIEGL VMX-450 deploys two rotating laser scanners, configured as a “Butterfly” (or “X”) pattern. Therefore, the point clouds measured by two scanners are in slant reticulated pattern as shown in Figure 3.4 (b).

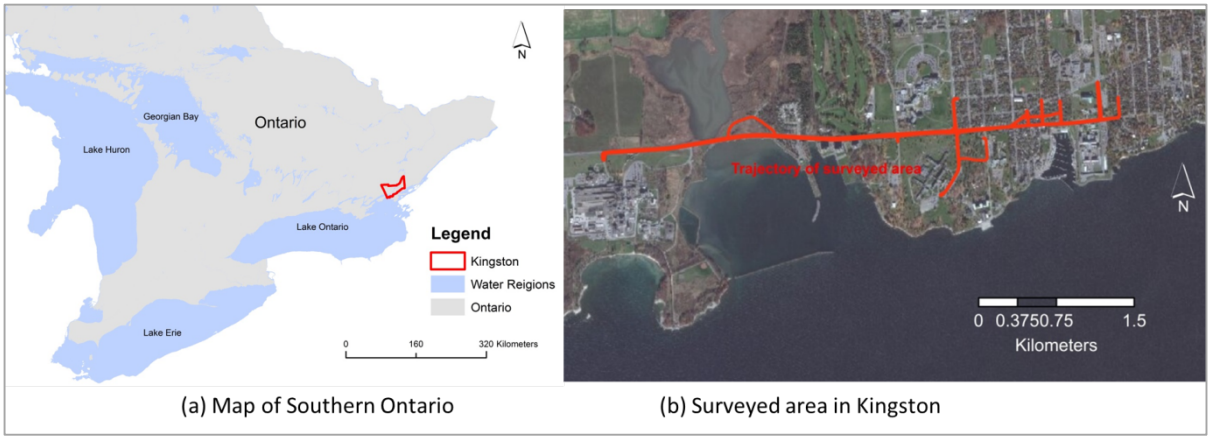

Figure 3.2: Study area.

In total, over 916 million points were collected and stored in 45 LAS files, which took up 23.8 GB of storage space and were generated by TerraScan Software. For all tiles, the point density is over 4800 points/m^2 , and some of them reach 5000 points/m^2 . All point cloud files have two return pulses. The speed of the vehicle was around 20-30 km/h during the survey. The entire area was measured five times for the two directions of the road. That means there are at least twice two-directions observations stored in the dataset. For example, as shown in Table 3.1, with each additional survey, the point density of Sample 3, which is a 50 m long road segment, increases, and the average spacing between points decreases. The images generated by the CCD cameras were saved in JPEG format, and all images take around 10 GB of storage space and include one CSV file containing the origin and direction coordinates, timestamp, roll, pitch, and yaw information, which can be used for visual

interpretation and reference of point clouds.

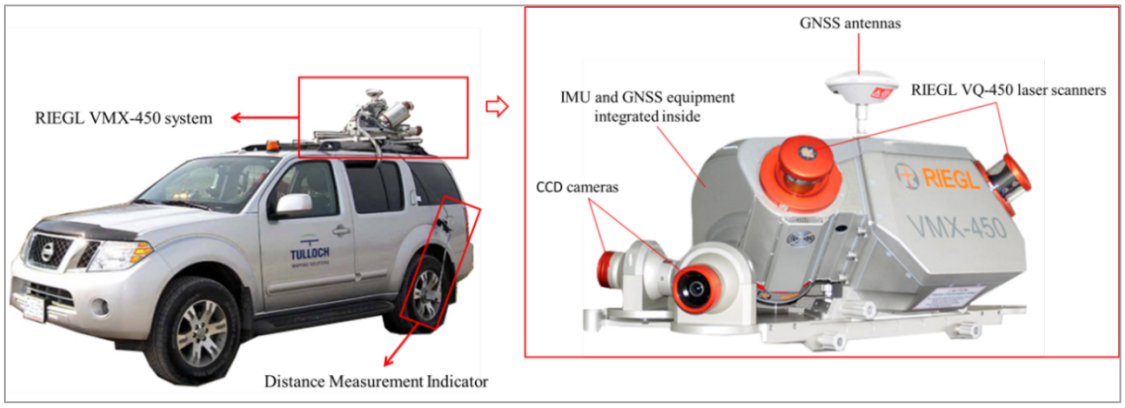

Figure 3.3: A RIEGL VMX-450 system

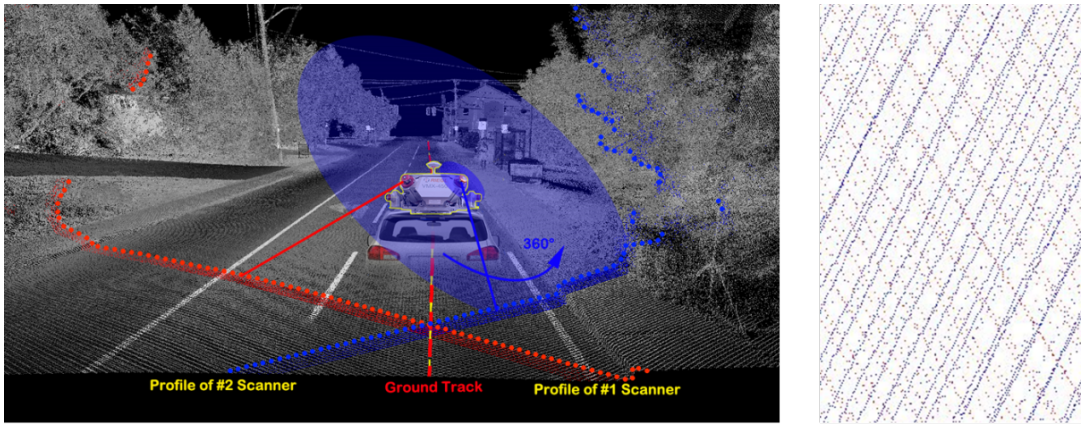

Figure 3.4: Illustration of (a) VMX-450 scanning pattern, and (b) Reticulated point clouds.

Table 3.1: Characteristics of point clouds by different acquisition missions for Sample 3.

Surveyed Times	Direction Number	Point Number	Points Density (points/m²)	Spacing (cm)
1	1 (East to West)	3,390,048	926.24	3
2	2 (East to West Then West to East)	6,877,517	1750.9	2
4	2 (East to West Then West to East)	17,652,231	4251.5	2
5	2 (East to West Then West to East)	20,743,822	4976.92	1

3.2.2 Reference Dataset

In order to obtain check points for validating the accuracy of final results, a field survey was carried out on September 4 and 5, 2015. Based on the National Standard for Spatial Data Accuracy (FGDC, 1998), at least 20 sample points should be selected as check points. In this study, total 30 check points were randomly chosen from the area covered by MLS dataset and surveyed by two Leica Viva GS14 GPS receivers: one base station and one rover, see Figure 3.6 (a) and (c).

All these check points (see Figure 3.5) were measured using the Real Time Kinematic (RTK) technique, and they should be at least one level more accurate than the system (RIEGL VMX-450) is tested. In Figure 3.6, (a) shows the GPS base station, (b) benchmark, (c) the GPS rover receiver used in the field survey. Table 3.2 lists the information of the permanent benchmark 75U501 adopted in the field surveys. This benchmark was established by the Geodetic Survey Division of Natural Resources Canada. Ellipsoidal heights determined by GPS were converted to orthometric height based on the height of geoid defined in the Height Reference System Modernization by the Natural Recourses Canada (2015). Meanwhile, there were additional 20 different feature points (see Figure 3.5) were surveyed to check the difference between the measured points and the original MLS points. All surveyed points were in projection North American Datum of 1983 (NAD83) Universal Transverse Mercator (UTM) zone 18N, and the vertical datum is the Canadian Geodetic Vertical Datum of 1928 (CGVD28). All surveyed points were post-processed regarding a base station with a mean base-line length of less than 3 km.

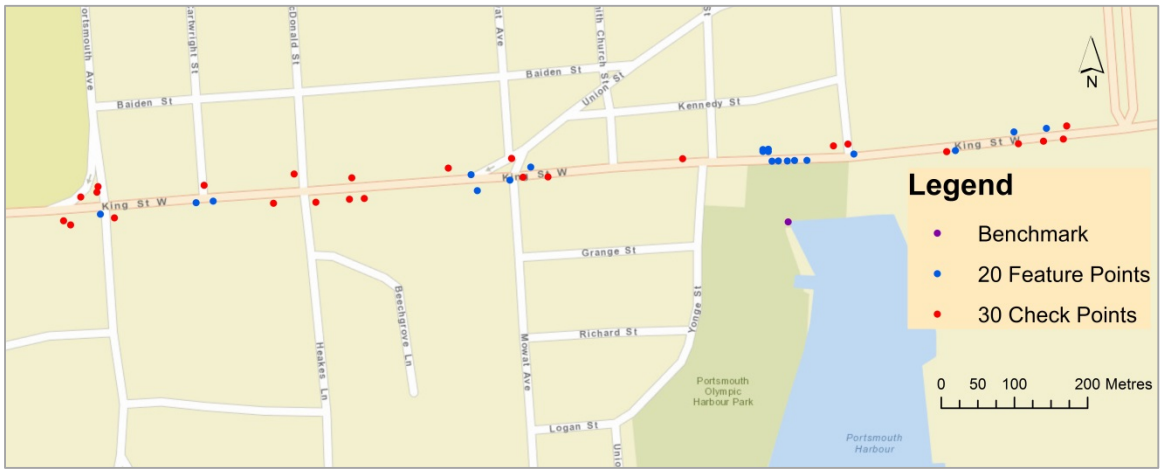

Figure 3.5: Check points and feature points.

Table 3.2: Benchmark used in the field work.

Benchmark	Vertical Datum	Elevation (m)	Reference Frame	Zone	Easting (m)	Northing (m)
75U501	CGVD28	75.990	NAD 1983	UTM18N	378851.159	4897458.583

Figure 3.6: Field surveys. (a) is the GPS used as the base station, (b) is the benchmark 75U501, and (c) is the GPS used as the rover in the survey.

3.2.3 MLS Data Quality Assessment

To validate the overall performance of MLS point clouds generated by RIEGL VMX-450, a set of feature points was collected. All feature points were chosen at corner points of objects along the street (e.g. short concrete walls or road edges) which can be conveniently identified in the point clouds. As shown in Table 3.3, the Root Mean Square Error (RMSE) of differences between MLS data and ground survey of vertical and horizontal directions are 4.1 cm and 29.3 cm, respectively. The standard deviation of the vertical difference is 3.6 cm, and horizontal difference standard deviations are 17.6 cm and 19.2 cm in X and Y direction, respectively. In this study, X and Y directions indicate the easting and northing directions in the NAD83 UTM zone 18N coordinator system, respectively. Considering the high differences in horizontal directions, a higher error rate may occur of the quantitative evaluation results in the external accuracy assessment in this experiment

Table 3.3: Positional differences between RTK surveyed feature points and MLS data.

	RMSE	Standard Deviation	
Vertical Direction(cm)	4.1	3.6	
Horizontal Direction(cm)	29.3	X	Y
		17.6	19.2

3.3 Pre-processing of Datasets

Sometimes, laser scanner can falsely measure and detect some points which do not actually exist as outliers. This can be due to the laser beam splitting at the edge of an object or a person or object moving in the scene during scanning. There are two types of outliers: low and high outliers (Sithole, 2004). Most low outliers (see Figure 3.7) are caused by multi-path errors and hits in the wall. Since the proposed filter requires the value of local lowest

voxel, low outlying points can produce errors in later processing steps. Thus, it is critical to identify and remove them. If low outliers cannot be removed from point clouds before applying the filter, they and their neighbour voxels will be wrongly classified. Some ground points could be misclassified into non-ground points (see Figure 3.8).

There are some existing methods can be used to detect low outliers. Meng et al. (2010) applied the Delaunay Triangulation method to compare each point to the local elevation reference to detect the outlier. This method was originally developed for ALS data which requires a pre-defined local elevation reference. However, for MLS point clouds, defining local elevation reference can be challenging in certain situations. As shown in Figure 3.7, some low outliers are under the road curb which are critical to determine the thresholds. Manual examination is another effective method to remove low outliers (Wang et al., 2009), but it is time consuming and not labour effective.

In this study, the Statistical Outlier Removal (SOR) algorithm is used to detect the outliers. Walsh and Hajjar (2009) applied the SOR algorithm into their study, and they obtained satisfactory results by this method. The SOR method first needs to determine the neighbourhoods. K nearest neighbours approach assigns the number of points to be included (Hoppe et al., 1992; Vanco and Brunnett, 2004; Rabbani et al., 2006). First, it guarantees that each neighbourhood will be determined by the same number of points regard thinking the point density. Then, the average distance of each point is computed. It considers the K nearest neighbours for each K as the first parameter, and the second parameter is the standard deviation multiplier which is a number of times the standard deviation. Assuming that the

result fit Gaussian distribution with a mean and a standard deviation, all points' mean distances are outside of an interval which defined by the global distances mean and standard deviation is recognized as outliers. After several tests in this study, the parameter combination which the number of neighbours is 8 and the standard deviation multiplier sets as 4 has the best performance of removing low outliers. Those removed noises might not be real outliers. But considering MLS data are very high density, those wrongly removed points will not affect the final result.

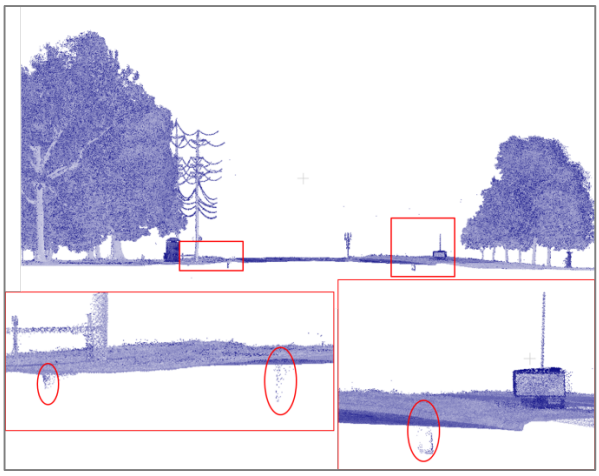

Figure 3.7: Low outliers in mobile laser scanning point clouds.

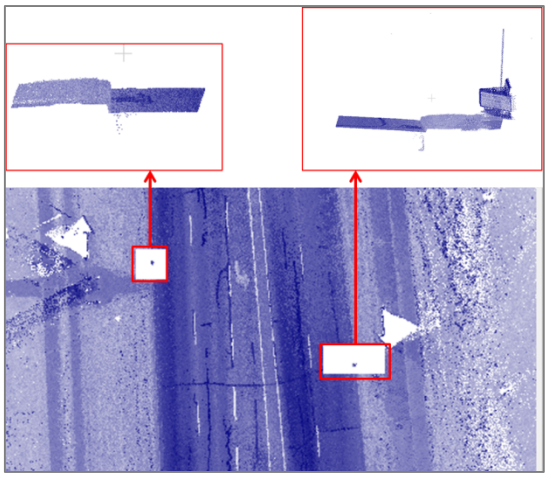

Figure 3.8: Misclassification caused by low outliers.

3.4 Filtering Ground Points

The literature review in Section 2.3 revealed the limitations of the existing filters to efficiently process point clouds, which are high in density, high in volume, and with complex terrain features, especially in urban areas. A voxel-based upward growing algorithm was firstly proposed by Yu et al. (2015b) for removing ground points to reduce computational time and solve difficulties of 3D objects detecting. This method was selected and applied to

rapidly and correctly generate ground points from MLS data in this thesis.

Figure 3.9 shows the workflow of the voxel-based upward growing algorithm for filtering terrain point clouds. There are three steps of this semi-automated algorithm, which requires input a set of the user-defined parameters. To begin with segmentation of the input raw MLS point clouds, the dataset can be divided and stored into different data blocks. Then, the data blocks will be voxelized using the octree index structure. Finally, to filter ground points, the proposed criteria will be applied into the voxelized point clouds and determined whether they are ground points or non-ground points.

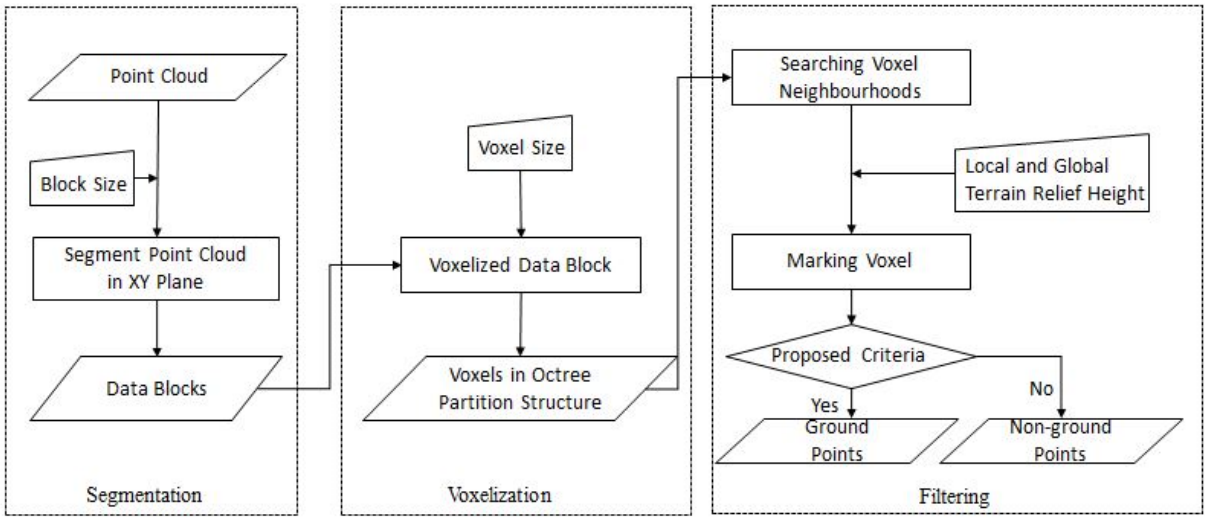

Figure 3.9: Workflow for filtering terrain points.

3.4.1 Segmentation of Point Cloud Scene

In the real world, the terrain has different reliefs in different areas. MLS point cloud scenes have much more details than ALS point clouds to represent the actual terrain. The raw point clouds contain huge number of points and large terrain relief. Therefore, processing the

whole point cloud scene as one part is more time consuming than segmentation the dataset into small pieces. In addition, this will also cause the filter loses effectiveness in ground points detecting which area has huge fluctuate terrain.

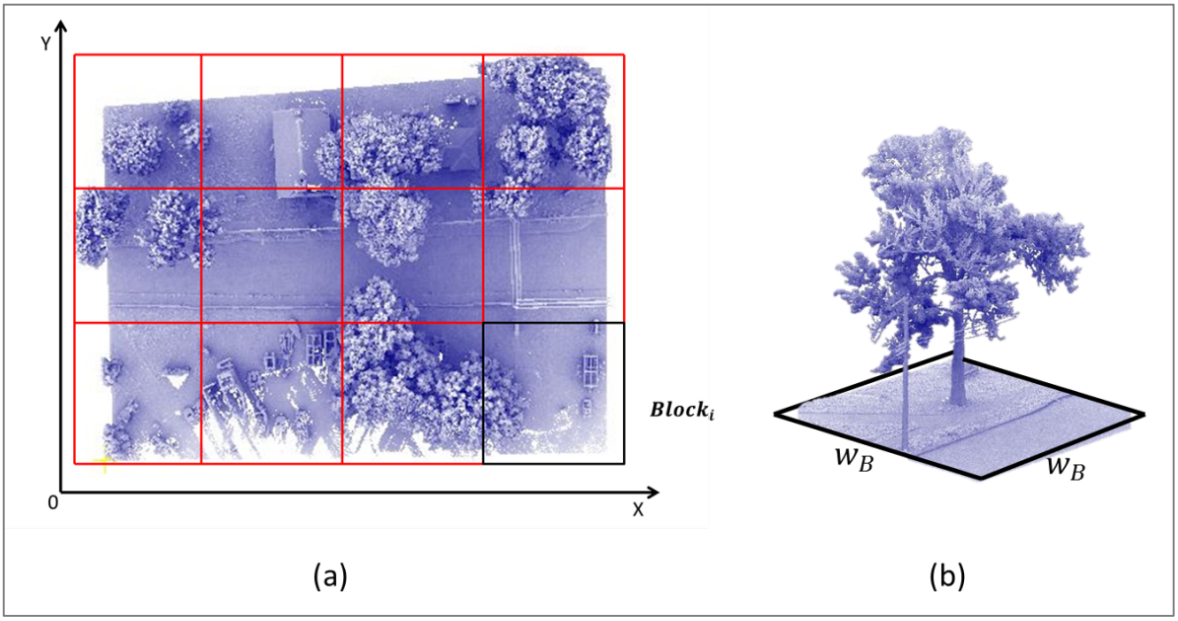

Figure 3.10: Illustration of raw point clouds segmentation and data block. (a) Top view of point clouds being segmented into data blocks, and (b) Data in $Block_i$.

To achieve better computational efficiency and filtering performance, first, the 3D point cloud scene was segmented into data blocks. As shown in Figure 3.10 (a), the large MLS data scene is vertically divided into a set of data $Block_i$, $i = 1, 2, 3, \dots, n_B$, (n_B is the total number of blocks in this scene) with a size of w_B in the XY plane. X is easting direction, and Y is northing direction. Figure 3.10 (b) shows a sample of a segmented data block. After segmenting the raw MLS data into data blocks, during the computation stage each data block will be processed separately to detect terrain points.

3.4.2 Voxelization of Point Clouds

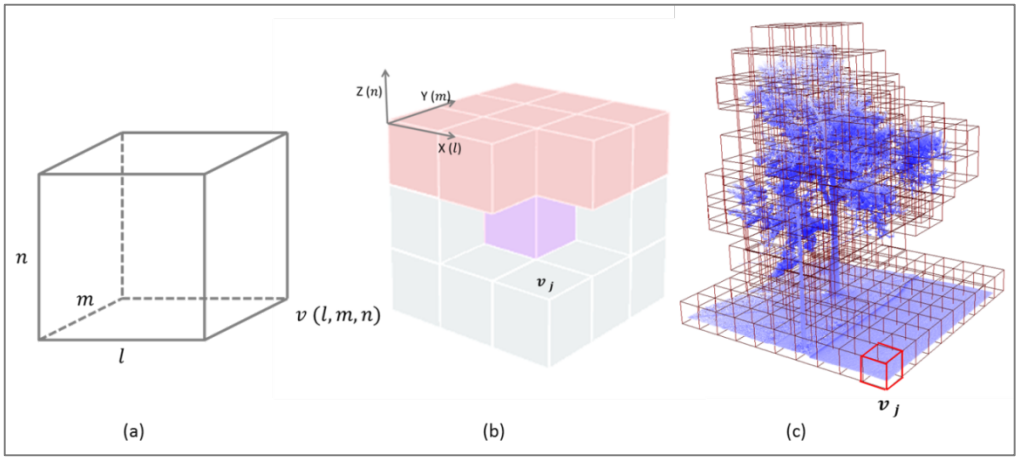

Figure 3.11: Illustration of (a) a voxel, (b) the voxelization, and (c) a sample of voxelized $Block_i$.

The second step is voxelization of each data block. A is cuboid shape data structure, and it is represented as voxel $v(l, m, n)$, see Figure 3.11 (a). A voxel can spatially conceptualize and represents as a set of volumetric elements (Wu et al, 2013). In this study, a voxel $v_j, j = 1, 2, 3, \dots, n_V$, (n_V is the number of voxels in $Block_i$) represents as a group of point clouds and sets as a cube shape which $l, m, and\ n$ have equal value w_V. In order to speed up the indexing of large amounts of unorganized 3D voxels, see Figure 3.11 (b), a voxel grid coordinate system is constructed using octree structure, see Figure 3.11 (c) (Xu et al, 2015). Recent years, there are many studies applied octree data structure into point clouds processing show that octree structure is very helpful in computation efficiency for 3D space decompositions (Barber et al., 2008; Elseberg et al., 2013; Linh and Laefer, 2014). To construct an octree structure, first, we need to calculate the bonding box of the point cloud $Block_i$, and initial the root node of this data block. Then sub-division of the octree is computed, and each node is divided into eight smaller nodes, which form as the voxelization

grid system as shown in Figure 3.12.

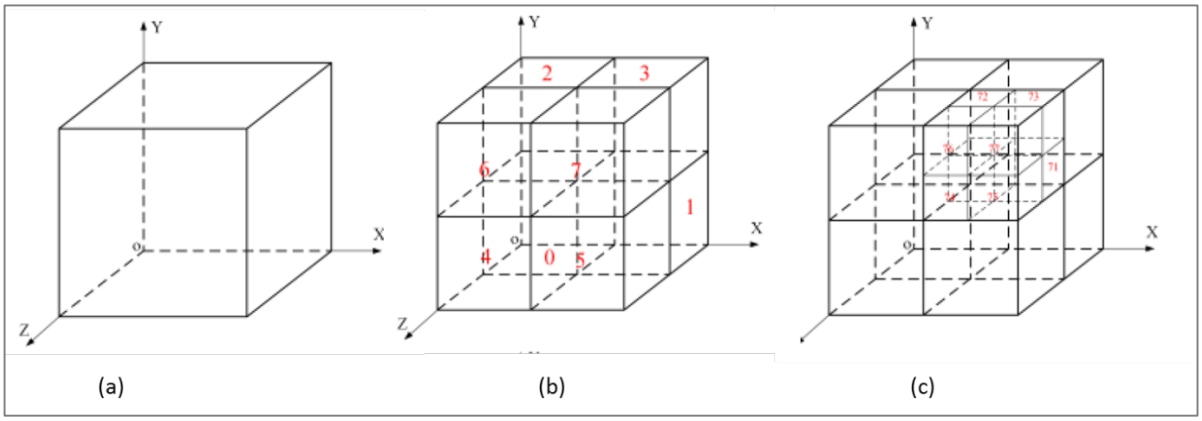

Figure 3.12: Process of constructing octree index structure to obtain the voxelization grid system.

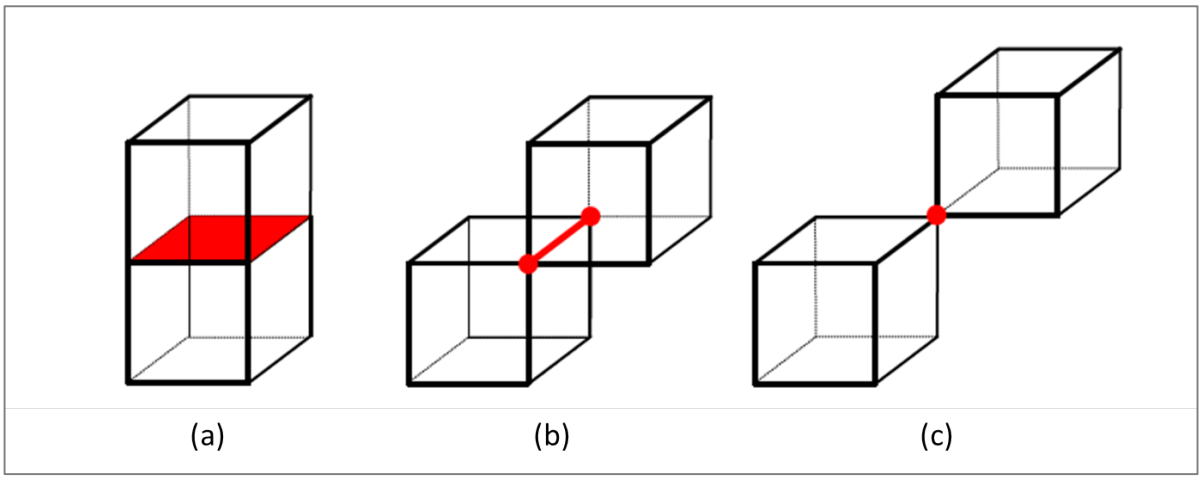

Figure 3.13: Three-type neighbours of a voxel in voxelization grid system. (a) Face neighbour, (b) Edge neighbour, and (c) Vertex neighbour

3.4.3 Searching Voxel Neighbourhoods and Marking Voxels

By using the octree partition structure, each voxel has a maximum of 26 neighbourhoods in a 3D voxelization grid system. There are three types' of voxel neighbours: face neighbours, see Figure 3.13 (a), edge neighbours, see Figure 3.13 (b), and vertex neighbours, see Figure 3.13 (c). In this study, nine upper-layer neighbours are used for an

upward growing process including one-top faced neighbour, four upper-edge neighbours, and four upper-vertex neighbours. Firstly, each voxelv_j , $j = 1, 2, 3, \dots, n_V$, grows to nine upper-layer neighbours. Then, the same growing modus is used for all nine upper-layer neighbours to continually grow upward. Each one of the nine neighbours computes separately.

The growing process breaks when there are no nine upper-layer neighbours of the grown voxel. Then, the highest voxel in the grown data block is marked as v_h, where v_h has the highest elevation in this grown region. In addition, the local height h_l of point clouds is defined as the elevation difference between elevations of v_h and the lowest elevation voxel v_l in the same data $Block_i$. At the same time, the global height $h_g$of point clouds is defined as the elevation difference between elevations of v_h and the lowest elevation voxel v_l in the data scene. Finally, in order to filter terrain points, all voxels $v_j$in this scene are labeled as terrain voxels which contain terrain points and off-terrain voxels which contain off-terrain points based on following criteria:

(1) Setting a local terrain relief height as H_l for the data block. This parameter constrains the maximum terrain relief heights of each data $Block_i$ in one scene.

(2) Setting a global terrain relief height as H_g for the point cloud scene. This parameter controls the maximum terrain relief heights of the whole scene.

(3) If the h_g of voxel v_j is less than H_g, and h_l is less than H_l, the voxel v_j will be regarded as an terrain voxel. All points in the voxel v_j are marked and kept as terrain points.

(4) If the h_g of voxel v_j is greater than H_g, or h_l is greater than H_l, the voxel v_j will be regarded as an off-terrain voxel. All points in the voxel v_j are marked and removed as off-terrain points.

3.5 DTMs Interpolation

After filtering the point clouds into terrain points and off-terrain points, the remaining task is the interpolation of ground points. Most interpolation methods produce similar results with high density dataset (Burrough and McDonnell, 1998). Since the point density of MLS data is very high, there is no need to apply the best predicated interpolation method. Rather than choose a more efficient method in computational performance and reduce the random errors (Shan and Toth, 2008). Based on the literature review in Section 2.4, a comparison of four interpolating methods is conducted to explore which one produces a better computational performance. They are IDW interpolation, Nearest Neighbour interpolation, Linear interpolation, and Natural Neighbour interpolation.

3.5.1 Inverse Distance Weighting Interpolation

Similar to other interpolation methods, IDW predicts the value at a point as a weighted average of the elevations at nearby reference points. Inverse Distance Weighted interpolation is an intuitive and efficient method and it has best result with evenly distributed points (Anderson, 2010). IDW interpolation assumes that the values of closest known locations have higher influences on estimated value than locations farther away (El-Sheimy et al. 2005). To predict the elevation of an unknown location, IDW weights reference points closer to the unknown point greater than farther points. The mathematical interpolation

function can be described by Equations 3.1, 3.2, and 3.3 (El-Sheimy et al. 2005):

$$Z(X,Y)_0 = \sum_{i=1}^{n} \lambda_i Z(X,Y)_i \tag{3.1}$$

$$\lambda_i = d_{i0}^{-p} / \sum_{i=1}^{n} d_{i0}^{-p} \tag{3.2}$$

$$\sum_{i=1}^{n} \lambda_i = 1 \tag{3.3}$$

where:

$Z(X,Y)_0$	is the elevation value of predicted location $(X,Y)_0$.
n	is the number of reference points surrounding the prediction location.
λ_i	are the weights applied to each reference point which decrease with
$Z(X,Y)_i$	is the elevation value of reference points at the location $(X,Y)_i$.
p	is the factor which determine how weights reduce by distance.
d_{i0}	is the distance between the location $(X,Y)_0$ and location $(X,Y)_i$.

The weights for the reference points applied in estimation are scaled. Therefore, the sum of the weights is equal to one. The power p can affect the weighting of the elevation of reference locations on the elevation of the predicted location. According to El-Sheimy et al. (2005), some practical experiences and studies have showed that a power equal to two produces better performance. Meanwhile, the value of power parameter is larger, the weight of nearby samples is heavier, and the estimated surface is more smooth (Li and Heap, 2014). Considering MLS data is very dense and this study tries to optimally keep terrain features, power p has been set as 2. In addition, to speed up the calculation process, it is common practice to limit the number of reference points (Johnston et al., 2001). Therefore, in this case,

the number of reference points n has been set as 12.

3.5.2 Nearest Neighbour Interpolation

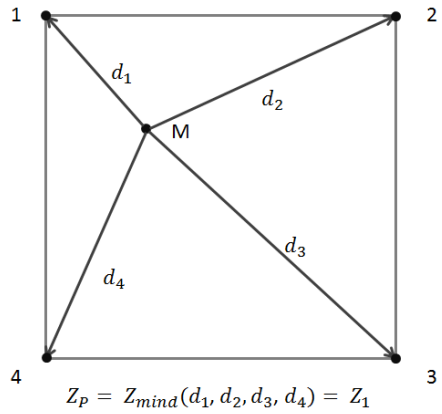

Figure 3.14: Example of Nearest Neighbour Interpolation.

Another interpolation method is used in this study is Nearest Neighbour. Nearest Neighbour interpolation method is a special case of IDW interpolation where p equals zero and n equals one (Laslett et al., 1987; Brus et al., 1996). This technique assigns interpolation point's value by substituting the value of its closest neighbour. Figure 3.14 is an example that illustrates the concept of comparing and calculating regular distributed neighbour points. Point M is the estimated point, and Euclidean distances between other four points and point M are d_1, d_2, d_3, and d_4. As shown in the diagram below, the distance d_1 has the shortest path of those four points. Therefore, the value of point M will be the value of point 1. The disadvantage of using this method is it is no error estimate. Only one of the sample points is considered in the estimate, and any other nearby sample points is excluded (Webster and Oliver, 2001). In other words, this method constructs a discontinuous surface with no smoothing process. However, the Nearest Neighbour interpolation is one of the most

computational efficient methods, and this is the main reason that it is applied in this study.

3.5.3 Linear Interpolation

The linear interpolation algorithm simulates the terrain surface by continuous Triangulated Irregular Network. The surface elevation is estimated by the elevation values at the nodes of the triangle where the predicted point is located. The interpolating points are calculated separately for each triangle. As a result, the interpolated value is not affected by the terrain behaviour of adjacent triangles (El-Sheimy et al. 2005). Linear interpolation assumes each triangle represents a planar surface (El-Sheimy et al. 2005).

There are two types of triangulation that can be used to triangulation: Delaunay conforming triangulation and Delaunay constrained triangulation. In this study, the TIN is firstly carried out by Delaunay conforming triangulation. Compared to constrained triangulations, Delaunay conforming triangulation contains fewer long and skinny triangles which are not satisfactory for some spatial analysis (ArcGIS, 2008). As Figure 3.15 describes, Delaunay triangulation first satisfies the requirements of Delaunay triangle criterion (Figure 3.15 [b]). All vertices in the triangulation are connected with a serial edge, and there is no vertex located within the inside of any circumcircles of each triangle in the triangulation as Figure 3.15 (c) shows (Gallant, 2000). After this triangulation has been completed, the predicted point's elevation can be calculated by linear interpolation as Equations 3.4 and 3.5 (Leberl, 1973).

$$Z(X,Y) = a_0 + a_1X + a_2Y \tag{3.4}$$

$$\begin{bmatrix} Z_A \\ Z_B \\ Z_C \end{bmatrix} = \begin{bmatrix} 1 & X_A & Y_A \\ 1 & X_B & Y_B \\ 1 & X_C & Y_C \end{bmatrix} \begin{bmatrix} a_0 \\ a_1 \\ a_2 \end{bmatrix} \tag{3.5}$$

where $Z(X,Y)$ is the elevation of predicted point, $X, Y, and\ Z$ of nodes $A, B, and\ C$ of the Delaunay triangle are used to calculated for the coefficients (a_0, a_1, a_2). The linear interpolation only works on the three nodes of the triangle within which the predicted point lies. Thus, the computation process is very efficient.

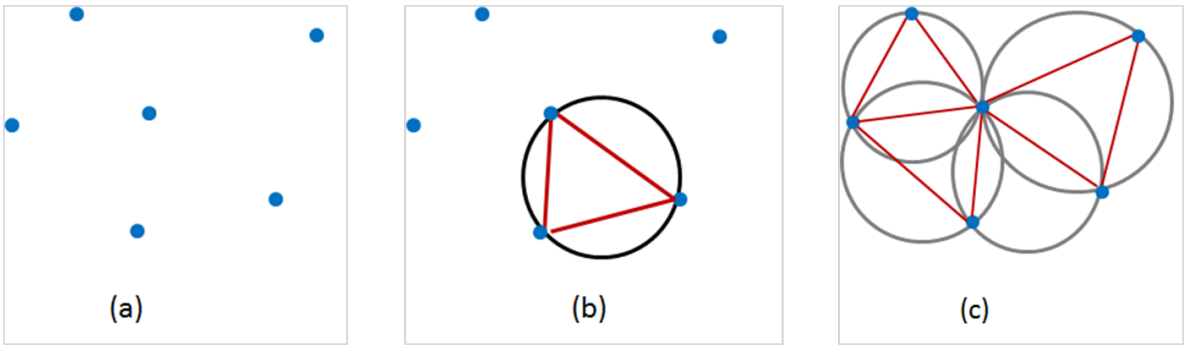

Figure 3.15: Illustration of (a) A collection of points, (b) A Delaunay triangle, and (c) A Delaunay triangulation.

3.5.4 Natural Neighbours Interpolation

The last interpolation method is Natural Neighbour. Natural neighbour interpolation finds the closest neighbour reference points to a predicted point and applies weights based on proportionate areas or volumes to the interpolate height value (Sibson, 1981). According to Watson (1992), Natural Neighbours interpolation method performs equally with both regularly and irregularly distributed data. Similar to Linear interpolation using Delaunay

triangulation data structure, the Natural Neighbours interpolation is calculated based on Voronoi diagram which is double to the Delaunay triangulation of the same set of points. Figure 3.16 describes the natural neighbours of point M associated with Voronoi polygons of the natural neighbours. Initially, the Voronoi diagram is produced from all known reference points p_i. Then a new Voronoi polygon, blue-colored polygon in Figure 3.16, is constructed around the predicted point M. The Natutal Neighbours interpolation is denoted by Equations 3.6 and 3.7 (Ledoux, 2005).

$$M(X,Y) = \sum_{i=1}^{n} w_i p(X,Y)_i \tag{3.6}$$

$$w_i = \pi_i(M)/\pi(M) \tag{3.7}$$

Similarly to all interpolation algorithms, Natural Neighbours interpolation applies the basic equation, as shown in Equation 3.6. The elevation of interpolated point M is calculated by relevant neighbours. However, all interpolation methods use different weights in the calculations. In the Natural Neighbours interpolation, weight w_i is the proportion of overlap areas $\pi_i(M)$ between this new polygon and the initial polygon and areas of initial polygons $\pi(M)$. Compared to distance-based interpolation method, such as IDW, natural neighbour interpolation assigns weights based on the percentage of overlapped area in Voronoi diagram. This approach theoretically could provide more accurate results.

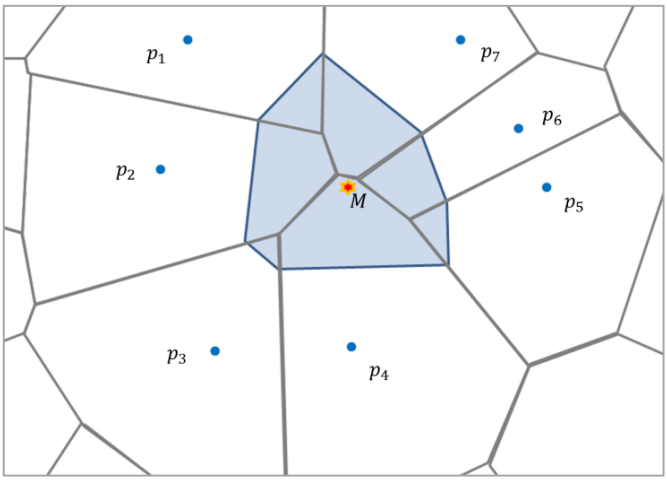

Figure 3.16: Example of Voronoi diagram of natural neighbours of point M.

3.6 Quality Assessment

Accuracy of spatial dataset is a kind of combination of positional accuracy and thematic accuracy (Congalton and Green, 2008). To derive a quality assessment of this study, there are two parts of accuracy assessments were carried out: accuracy assessment of filtering algorithm (thematic accuracy assessment) and accuracy assessment of DTMs (positional accuracy assessment).

3.6.1 Accuracy Assessment of Ground Filtering Algorithm

Thematic accuracy usually represents the differences between the labeled attributes of map features and the true attributes of real world features (Congalton and Green, 2008). Error matrix as the most wildly used method is applied into the thematic accuracy assessment (Congalton and Green, 2008). Table 3.4 shows the error matrix for binary classification, where tp is true positive, tn is true negative, fp is false positive, fn is false negative. In this study, tp and tn are the number of terrain points and off-terrain points that are correctly classified into each class, respectively. The fp means the number of off-terrain points is

incorrectly classified into terrain points. Similarly, fn means the number of terrain points is misclassified into off-terrain points.

Table 3.4: Error matrix for binary classification.

Class\ Classified	as Positive	as Negative
Positive	tp	fn
Negative	fp	tn

Three criteria are used to measure the accuracy in this study: overall accuracy, completeness correctness (Jwa and Sohn, 2012), Type I error and Type II error (Sithole and Vosselman, 2003).

Overall accuracy is obtained by

$$overall\ accuracy = \frac{tp+tn}{tp+tn+fp+fn} \tag{3.8}$$

Completeness (omission error, producer's accuracy) is obtained by

$$completeness = \frac{tp}{tp+fn} \tag{3.9}$$

Correctness (commission error, user's accuracy) is obtained by

$$correctness = \frac{tp}{tp+fp} \tag{3.10}$$

Type I error is the error which incorrectly identified terrain points as off-terrain points, which is obtained by:

$$Type\ I\ error = \frac{fn}{tp+fn} \tag{3.11}$$

Type II error is the error which incorrectly identified off-terrain points as terrain points, which is obtained by:

$$Type\ II\ error = \frac{fp}{fp+tn} \tag{3.12}$$

In this study, the error matrix is used for evaluating the performance of voxel-based upward growing algorithm. Reference data are five sample areas manually labeled in CloudCompare by visual interpretation. The five samples were chosen by their features including the terrain relief and off-terrain objects. Each sample point cloud was segmented into 10 cm width profile based on easting direction for easily visual interpretation as Figure 3.17 shows. The details of five sample datasets are shown in Table 3.5. Both Samples 3 and 4 are area with a large topographic relief. Sample 3 has a large relief along the direction of road; while, Sample 4 has much vegetation on steep slope (greater than 45°) which is similar with forest in mountain areas. Samples 1, 2, 3 and 5 are typical urban areas with common features such as small and large buildings, traffic signs and facilities, vehicles, vegetation, fire hydrant and power facilities. The average distance between the road centre line and the furthest point, which MLS system can observed, is 40 m.

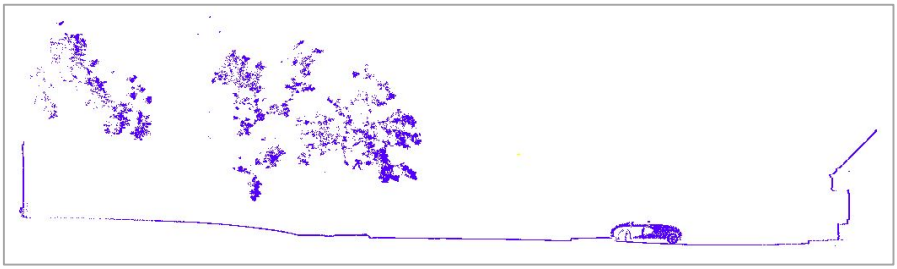

Figure 3.17: A profile sample for visual interpretation.

Table 3.5: Details of labeled sample sites.

Test Sample	Number of Points	Point Density (points/m²)	Measured Times	Terrain Points	Off-terrain Points	Length (m) (along the road)	Data Volume (Mb)	Features of Scene
Sample 1	8113459	2085	4	6715596	1397863	50	263	Small topographic relief, railway with trains, lower vegetation, and trees
Sample 2	9808121	2270	4	1963354	7844767	50	318	Small topographic relief, large building, and lower vegetation
Sample 3	18792025	4930	5	11941705	6850320	50	609	Moderate topographic relief, houses, vehicles, traffic signs, vegetation, and power lines and poles
Sample 4	25384615	4639	4	16918577	8466038	100	823	Large topographic relief, steep slope with vegetarians, large buildings, low concrete walls
Sample 5	31817216	4171	3	20046257	11770959	100	1024	Small topographic relief, houses, power lines and poles, vegetation

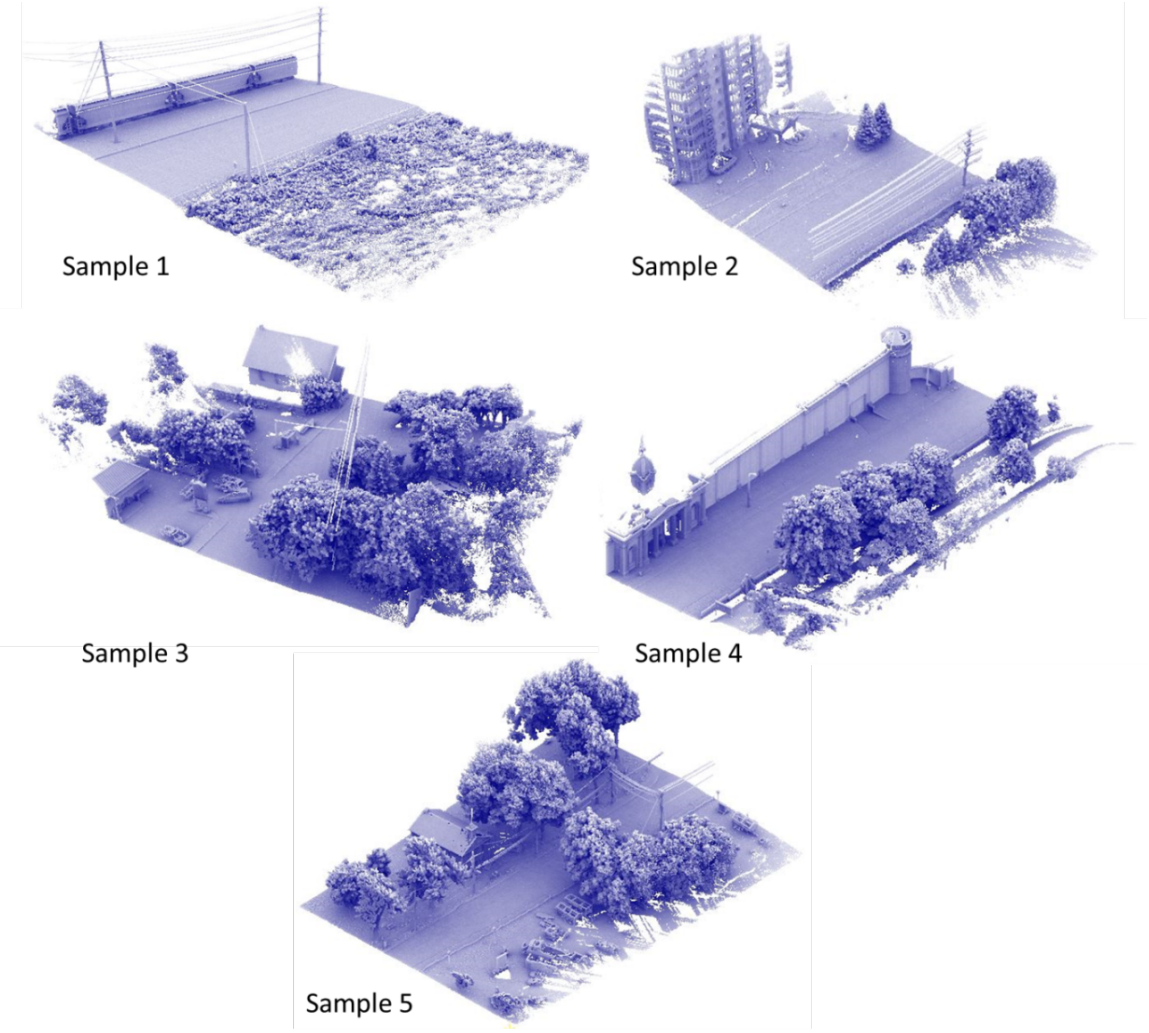

Figure 3.18: Sample Scenes of raw point clouds.

3.6.2 Accuracy Assessment of DTMs

Positional accuracy reflects and measures how different between a location of a spatial feature on the map and a reference location on the ground (Bolstad, 2005). In this study, the vertical position accuracy of DTM is validated by several statistical parameters including RMSE, arithmetic mean, standard deviation of population of vertical errors, standard error of estimates of RMSE. According to some previous positional accuracy assessment theories (Greenwalt and Schultz, 1962; Mikhail and Gracie, 1981; Congalton and

Green, 2008), all these statistical parameters are calculated by the following equations. The vertical RMSE of the sample of vertical errors (e_{vi}) is estimated by

$$RMSE_v = \sqrt{\sum_i^n (e_{vi})^2 / n} \tag{3.13}$$

where

$$e_{vi} = v_{ri} - v_{mi} \tag{3.14}$$

v_{ri} equals the reference elevation at the ith check point, v_{mi} equals the DTM elevation at the ith check point, and n is the number of sample.

The arithmetic mean of the absolute error values is calculated by

$$\overline{|e_v|} = \sum_i^n |e_{vi}| / n \tag{3.15}$$

The standard deviation S_v of the population of vertical errors is estimated by

$$S_v = \sqrt{\sum_i^n (e_{vi} - RMSE_v)^2 / (n-1)} \tag{3.16}$$

and the standard error of estimates of $RMSE_v$ is estimated by

$$S_{RMSE_v} = S_v / \sqrt{n} \tag{3.17}$$

Assuming that the population of positional error is normally distributed, and Z_i is the value from the x-axis of ith standard normal distribution at the probability level. The vertical accuracy can be represented by two standards (Congalton and Green, 2008): the interval of errors around RMSE which includes 95% of map errors is $RMSE \pm Z_i S_v$, and a confidence interval around the estimate of RMSE at 95% probability is $RMSE \pm Z_i S_{RMSE}$. Here the Z_i

equals 1.96 which is the standard normal distribution Z statistic for an interval with probability of 95%.

During this step, two parts of assessment were carried out: internal accuracy assessment and external accuracy assessment. Based on a previous review of positional accuracy assessment (FGDC, 1998), at least 20 samples should be chosen for the statistical analysis. Hence, a number of 200 ground points were randomly chosen from the Sample 3 used into the cross-validation as the internal accuracy assessment. Meanwhile, the external accuracy assessment used the 30 GPS check points into the statistical analysis. All the positional accuracy assessments indicate the vertical accuracy which is the accuracy in Z direction or height.

3.7 Chapter Summary

This chapter introduced the entire procedure of generating DTM from MLS point clouds. Firstly, the details of study area and dataset were described. Secondly, a pre-processing stage was proposed to remove outliers from raw MLS point clouds. Then, the filtering process was carried out for separating terrain points from point clouds by using voxel-based upward growing algorithm. In this step, the point cloud was segmented and voxelized into pre-defined size. Then, all voxels applied the main function which satisfied with upward growing criteria. After filtering terrain points, four interpolation methods including IDW interpolation, Nearest Neighbour interpolation, Linear interpolation, and Natural Neighbours interpolation were proposed to efficiently derive a high quality raster format DTM. Lastly, the method of quality assessment of the entirety workflow was stated.

Chapter 4
Results and Discussion

This chapter presents the final results of DTM which was generated by the proposed method from MLS point clouds. Chapter four is organized into four sections. Section 4.1 includes the results of filtering processes, analysis of parameters used into the proposed filter, and quantitative and qualitative evaluation of the proposed algorithm. Section 4.2 shows the final delivered gridded DTMs of the study area. Section 4.3 presents the internal and external accuracy assessment of the gridded DTMs. Finally, Section 4.4 summarizes the main results of this chapter.

4.1 Quality of Ground Filtering

In this study, the filtering process is the first and the most important part separating the terrain points and off-terrain points. In this section, the proposed voxel-based upward growing algorithm was applied to five sample sites and performance was assessed both qualitatively and quantitatively. The visual interpretation process was conducted by CloudComapre v2.6.2 and TerraScan software (Evaluation Edition). The ground points of five sample datasets were validated by error matrix which was described in Section 3.6.1. The whole process of ground points filtering was implemented in C++ code in Microsoft Visual Studio 2010 and used some modules provided by Point Cloud Library (PCL) 1.6.0. A moderate configured laptop carried out this task with an Intel® Core™ i5-3320M 2.60 GHz processor with 8 GB memory random access memory (RAM), and uses Windows 7 64-bits operating system.

4.1.1 Parameters Analysis in Ground Filtering

4.1.1.1 Analysis of Block Size

In order to determine the optimal parameter combination and evaluated the sensitivity of these parameters, a series of experiments were carried out. To segment the scene into blocks the size w_B of $Block_i$ should be firstly defined. The purpose of segmenting point clouds into blocks is to reduce the computational time and improve the accuracy of the filter. At this stage, the voxel size w_V, the local terrain relief height as H_l and the global terrain relief height as H_g were set as 0.05 m, 0.4 m and 4.5 m, respectively. Segmentation was carried out at various, i.e. 1 m, 3 m, 5 m, 8 m, and 10 m. Since Samples 1 and 3 have exhaustive and different features as described by Table 3.5, they were used to test the parameter combinations.

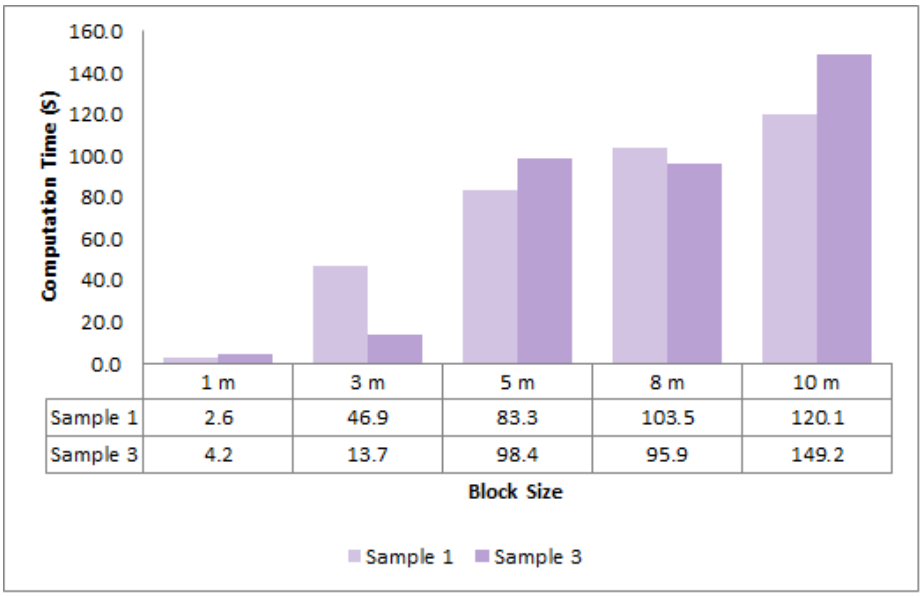

	1 m	3 m	5 m	8 m	10 m
Sample 1	2.6	46.9	83.3	103.5	120.1
Sample 3	4.2	13.7	98.4	95.9	149.2

Figure 4.1: Computational time of applying different block sizes.

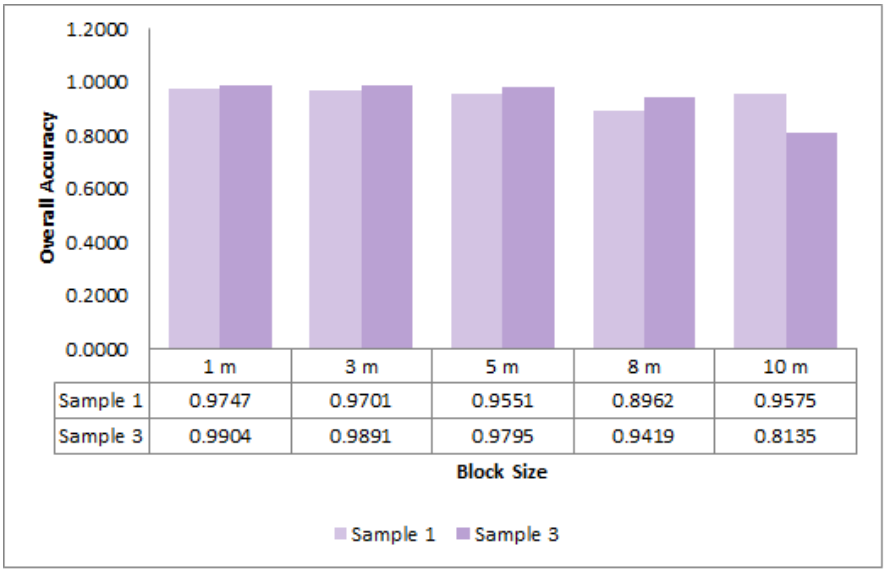

Figure 4.2: Overall accuracy of applying different block sizes.

Figures 4.1 and 4.2 present the computational time and overall accuracy of different block sizes. Figure 4.1 shows that the computational time exponentially increases as the block size increases. When the block size was set to 1 m, the whole algorithm only needed several seconds to process a 50 m long road dataset, e.g. 2.6 seconds for Sample 1 and 4.2 seconds for Sample 3, respectively. However, when the block size increases to 8 m, the processing time is increased to the hundred-second level, e.g. 103.5 seconds for Sample 1 and 95.9 seconds for Sample 3, respectively. The computational time reduced slightly for the 8 m block size of Sample 3 (95.9 seconds) compared to the 5 m block (98.4 seconds). That can be explained by the various internal process performance of computer such as RAM space. Similarly, Figure 4.2 illustrates the overall accuracy of applying various block sizes, ranging from 0.8 to 0.99. It is noticeable that with the overall accuracy of 10 m block size for Sample 1 (i.e. 0.9575) is higher than that of 5 m (i.e. 0.9551) and 8 m block size (i.e. 0.8962).

That may be caused by other fixed parameters which are not suitable to this scene. The above analysis indicated that the ground filtering overall accuracy decreases when block size increases.

4.1.1.2 Analysis of Voxel Size

Theoretically, the voxel size affects the accuracy of detecting the terrain points and influences the computing time of upward growing. A fixed parameter combination was used to explore the influences of voxel size, i.e. block size $w_B = 3$ m, the local terrain relief height $H_l = 0.4$ m, and the global terrain relief height $H_g = 4.5$ m, respectively. Same with the previous section, Samples 1 and 3 were used in this analysis.

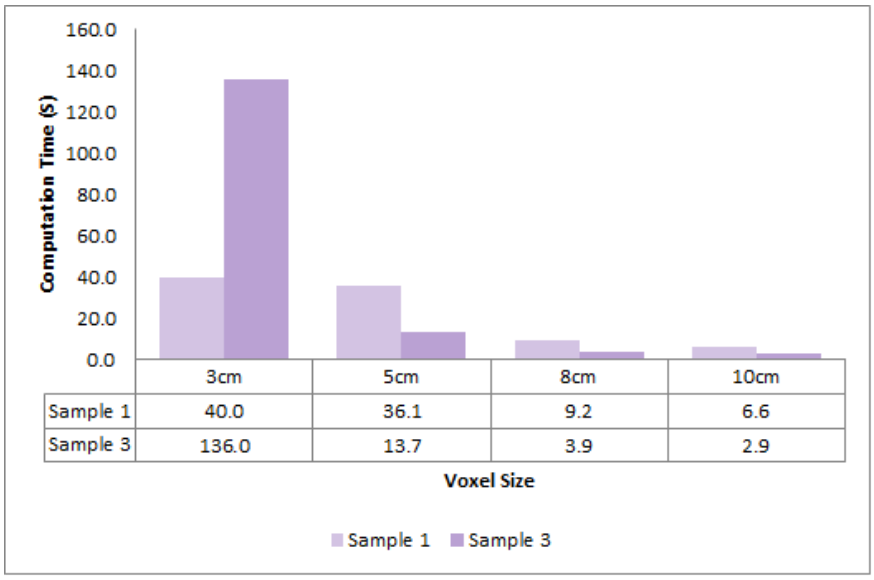

	3cm	5cm	8cm	10cm
Sample 1	40.0	36.1	9.2	6.6
Sample 3	136.0	13.7	3.9	2.9

Figure 4.3: Computational time of applying different voxel sizes.

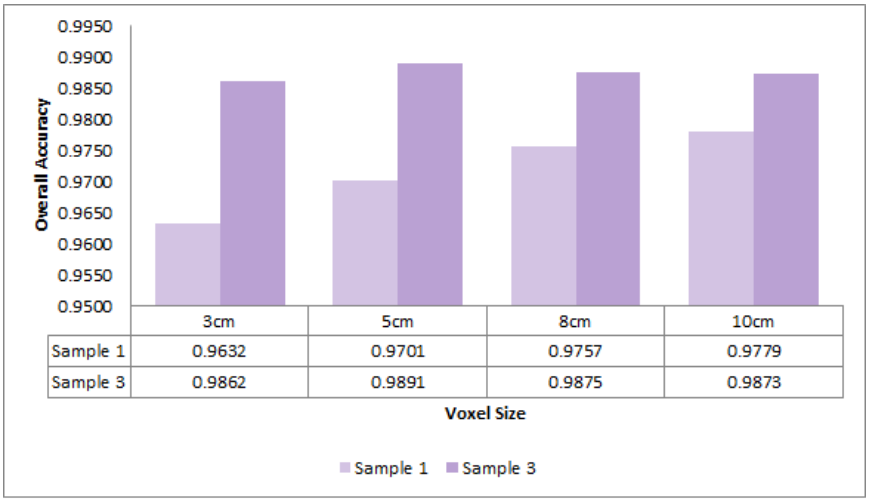

Figure 4.4: Overall accuracy of applying different voxel sizes.

Figures 4.3 and 4.4 present the computing time and overall accuracy for different voxel sizes setting. As the voxel size increases, the computational time reduces significantly from 40.0 seconds to 6.6 seconds for Sample 1 and 136.0 seconds to 2.9 seconds for Sample 3. The large difference in computational time of these two sample sites is caused by the point density. Table 3.5 shows the point density of Samples 1 and 3 were 2,085 and 4,930 points/m^2, respectively. In addition, the overall accuracy of various voxel sizes setting is different. The overall accuracy for Sample 1 increases as the voxel size increases. In contrast, the overall accuracy for Sample 3 is a normal distribution and maximized at 5 cm voxel size. Hence, there is no significant trend can be concluded for the overall accuracy of different voxel sizes. The presumable reasons are 1) there are other parameters affecting the final result, and 2) different terrain features can influence with the accuracy.

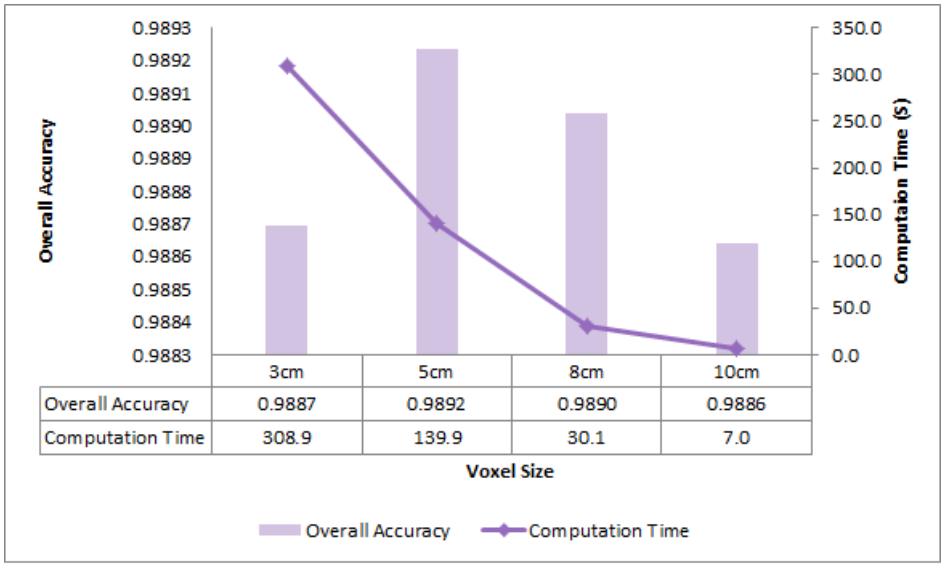

Figure 4.5: Overall accuracy and computing time of Sample 5 with different voxel sizes.

Theoretically, smaller voxel size should produce higher accuracy since the algorithm classifies the whole voxel into terrain points and off-terrain points. Therefore, Sample 5 was applied with the same test and the results are presented in Figure 4.5. Sample 5 has the same trend as Sample 3 in terms of the overall accuracy and computing time. Different from the theoretical assumption, the 3 cm voxel size has lower overall accuracy and more computational time. This is due to the voxel size is smaller than the terrain surface, which results in many terrain points classified to the off-terrain category. In addition, more analysis was carried out with Sample 1. Both Types I and II error of Sample 1 using the same parameter setting were calculated as listed in Table 4.1. Type I error is the terrain points falsely detected as off-terrain points, and they increase as the voxel size increases. While Type II error significantly decreases as the voxel size increase. As shown in Figure 3.18, Sample 1 contains much lower vegetation cover. Smaller size voxel on grass can be easily classified to the terrain part. Meanwhile, even for manually interpretation, lower vegetation

cover is a big problem. It is difficult to determine if they are vegetation points or terrain points. Thus, the labeled points may have some errors, which is another reason for this phenomenon. Hence, it can be concluded that the 5 cm voxel size setting is a global thresholding of the voxel-based upward growing algorithm for filtering ground points from MLS data.

Table 4.1: Types I and II errors of Sample 1.

Voxel Size	3 cm	5 cm	8 cm	10 cm
Type I Error	0.0183	0.0185	0.0193	0.0182
Type II Error	0.1256	0.0846	0.0487	0.0406

To explore more about the relationship between block size and voxel size, several additional tests were conducted. Different combination of block sizes of 3 m, 5 m, 8 m, and 10 m and the voxel size of 3 cm, 5 cm, 8 cm, and 10 cm were used by the algorithm with fixed local terrain relief height $H_l = 0.4\,m$, and global terrain relief height $H_g = 4.5\,m$. Figure 4.6 and Figure 4.7 demonstrate a consistent pattern in terms of accuracy despite the changes to voxel size. It indicates that the changes of block size and voxel size affect the accuracy of filtering result.

The processing time increases when the block size increases for a fixed voxel size. On the contrary, with a fixed block size, the upward growing process is more efficient when the voxel size increases. In order to reduce the processing time for filtering terrain points from raw data, the block size should be set as small as possible; and the voxel size should be set as large as possible. Moreover, the voxel size cannot be too small or too large considering

its accuracy level. Therefore, the block size $w_B = 3\,m$ and voxel size $w_V = 5\,cm$ were chosen in this study to filter the terrain points, which is also can be a global threshold setting.

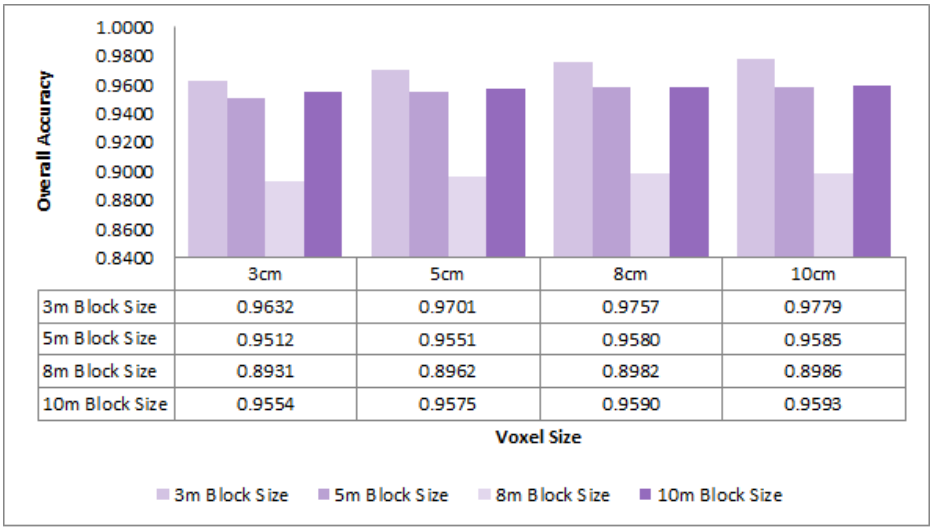

	3cm	5cm	8cm	10cm
3m Block Size	0.9632	0.9701	0.9757	0.9779
5m Block Size	0.9512	0.9551	0.9580	0.9585
8m Block Size	0.8931	0.8962	0.8982	0.8986
10m Block Size	0.9554	0.9575	0.9590	0.9593

Figure 4.6: Overall accuracy of different block sizes and voxel sizes for Sample 1.

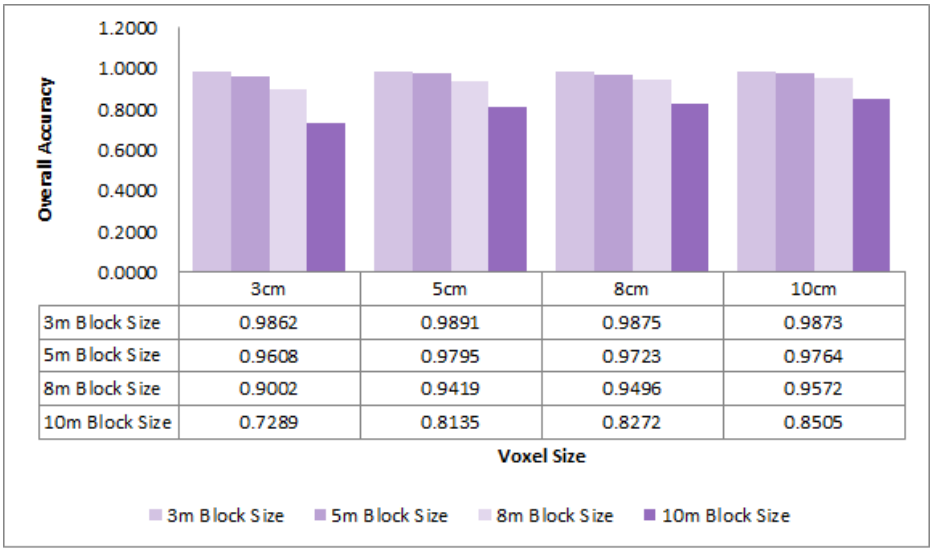

	3cm	5cm	8cm	10cm
3m Block Size	0.9862	0.9891	0.9875	0.9873
5m Block Size	0.9608	0.9795	0.9723	0.9764
8m Block Size	0.9002	0.9419	0.9496	0.9572
10m Block Size	0.7289	0.8135	0.8272	0.8505

Figure 4.7: Overall accuracy of different block sizes and voxel sizes for Sample 3.

4.1.1.3 Analysis of Local and Global Terrain Relief Height

Based on the concept of voxel-based upward growing algorithm, the local and global terrain relief heights only influence the accuracy of final results in terms of computational time. Therefore, a fixed block size of 3 m and voxel size of 5 cm were used to examine the appropriate local and global terrain relief heights. It requires prior knowledge of the terrain relief of the study area to define these two parameters. If the terrain changes a lot, both the local and global relief height should be set higher than an area with fewer terrain changes. The selected area is relatively flat. After visually exploring the point clouds, the local relief height ranges between 0.45 m and 0.65 m and the global relief height ranges between 4.5 m and 6.5 m.

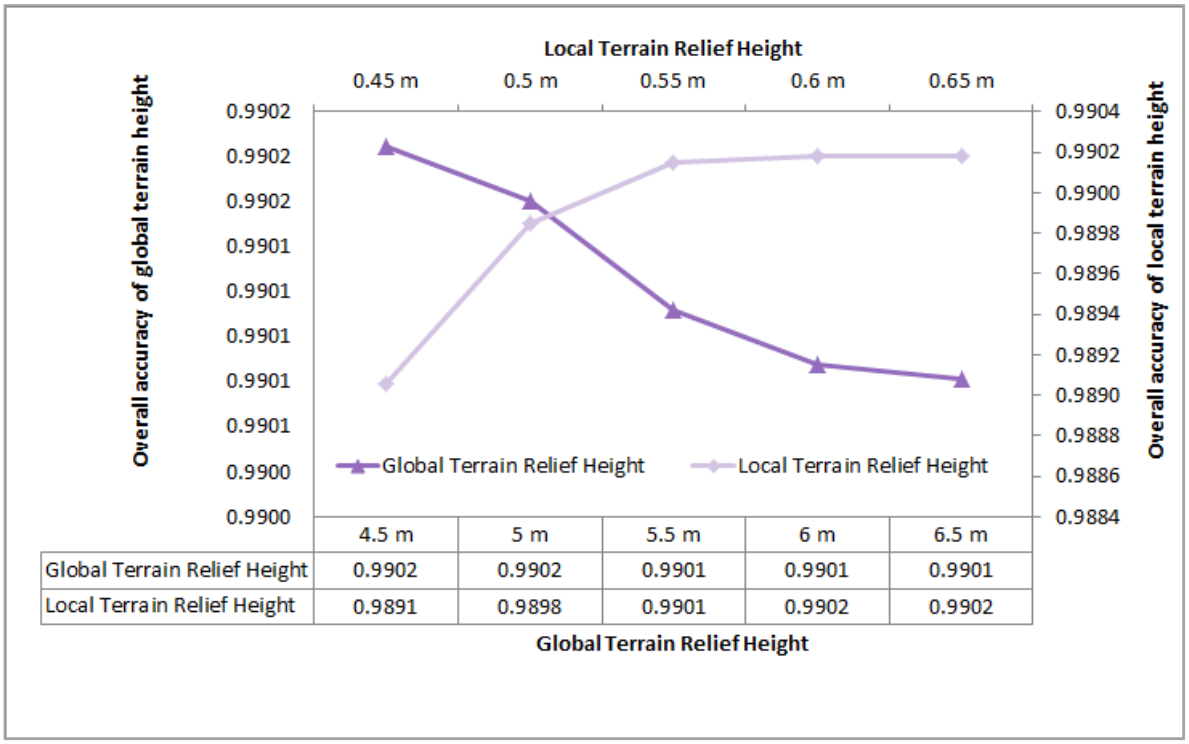

Figure 4.8: Overall accuracy of different local and global terrain relief height settings.

Hence, different terrain relief heights of the scene (i.e. 4.5 m, 5 m, 5.5 m, 6 m, and 6.5 m) were tested with fixed H_l= 0.45m for Sample 3. At the same time, a fixed H_g= 4.5 m was applied with different local terrain relief height (i.e. 0.45 m, 0.5 m, 0.55 m, 0.6 m, and 0.65 m). Figure 4.8 presents the testing results, which shows that the overall accuracy of filtering decreases as the global relief height increases for a fixed local terrain relief height. But if the global terrain relief height is not large enough, some ground surface will be categorized to off-ground points. Therefore, an optimal global relief height value should be chosen to achieve the best performance for the study area.

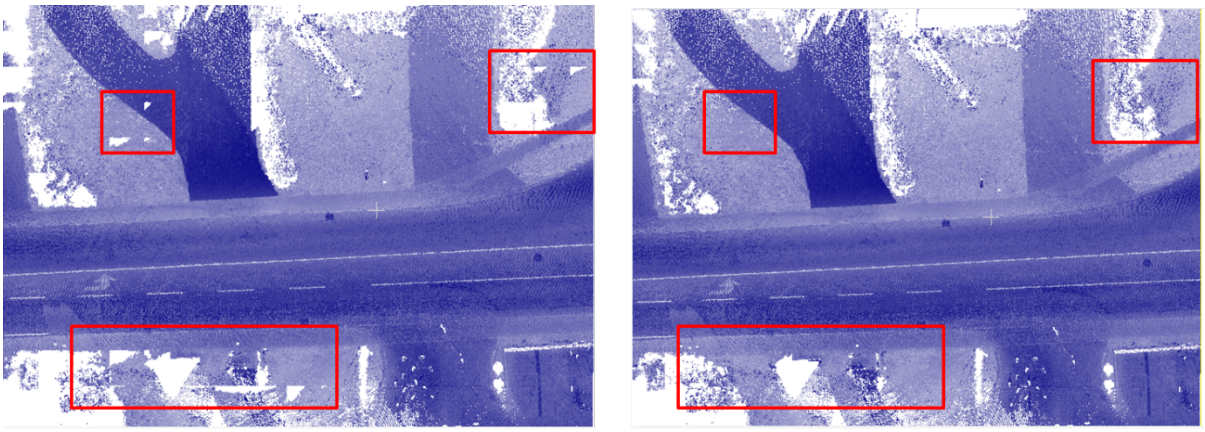

(a) H_l= 0.45m and H_g= 4.5m (b) H_l= 0.6m and H_g= 4.5m

Figure 4.9: Comparison of ground points filtering with different local terrain relief height settings.

On the contrary, the overall accuracy will reach a maximum value if the local relief height increases for a fixed global terrain relief height. After reaching the peak value, all points are classified to terrain and off-terrain categories. Meanwhile, if the local terrain relief height is not large enough, the terrain points can be classified into off-terrain points. For instance, Figure 4.9 (a) shows that areas in the red boxes have missing data which caused by

misclassifying the terrain points as off-terrain points when H_l= 0.45 m and H_g= 4.5 m. However, after increasing the local terrain relief height to 0.6 m as shown in Figure 4.9 (b), the situation significantly improved in the highlight areas. The same examination was carried out with Sample 2, and the final results present the same trend as Sample 3. Thus, a proper local terrain height should be set depending on different study areas.

4.1.2 Quantitative Analysis of Voxel-based Upward Growing Algorithm

Some misclassified terrain points which denote Type I error can be interpolated by their neighbourhoods; while an off-terrain point misidentified as terrain point will cause an inaccuracy of the interpolated DTM. Therefore, Type II error is another vital statistical value should be considerate.

Firstly, after analyzing various parameters of the voxel-based upward growing algorithm in the previous section, a set of global threshold was chosen and applied in all five sample sites. Figure 4.10 presents the ground points filtering results and accuracy assessment of five sample sites with w_B = 3 m, w_V = 0.05 m, H_l= 0.6 m, and H_g = 5.5 m. The left column of Figure 4.10 lists terrain points and the right column lists off-terrain points. Table 4.2 shows the lowest overall accuracy was Sample 4, i.e. 0.949, where an area with very steep slope. The overall accuracy of other sample sites ranges between 0.963 and 0.99. The average overall accuracy of these five samples is 0.975.

All these samples have correctness and completeness greater than 0.95. The average value of correctness and completeness were 0.980 and 0.986, respectively. Sample 1 has the largest Type II error than others. The main reason was discussed in Section 4.1.1.2. Both

improper parameter setting and visually misclassified terrain points result in the high Type II error rate as 0.166. In addition, Samples 3 and 5 have similar terrain features as typical urban scenes. Also, both of these two samples provide an excellent performance on accuracy assessment. Thus, in this case, the pre-defined thresholding set is not a global threshold for all data set, but it is suitable for the data with similar terrain relief and urban objects.

Several more suitable parameters were set for Samples 1, 2, and 4 to obtain higher accuracy in these cases. As previously discussed, Sample 1 is an area with much lower vegetation cover. As a result, there are many off-terrain points were misclassified as the ground which is denoted as a high rate of Type II error. But the overall accuracy, correctness and completeness are all greater than 0.95 which are acceptable. In this case, the main purpose of the sample filtering is to reduce Type II error rate. Considering there is much lower vegetation cover on terrain leading to high Type II errors, the slight reduction of the local and global terrain relief height is helpful. The same block and voxel sizes were set, and H_l= 0.4 m and H_g = 4.5 m. The overall accuracy, correctness, and completeness of the final results have increased to 0.97, 0.982, and 0.982, respectively. Type II error was significantly reduced from 16.57% to 8.46%.

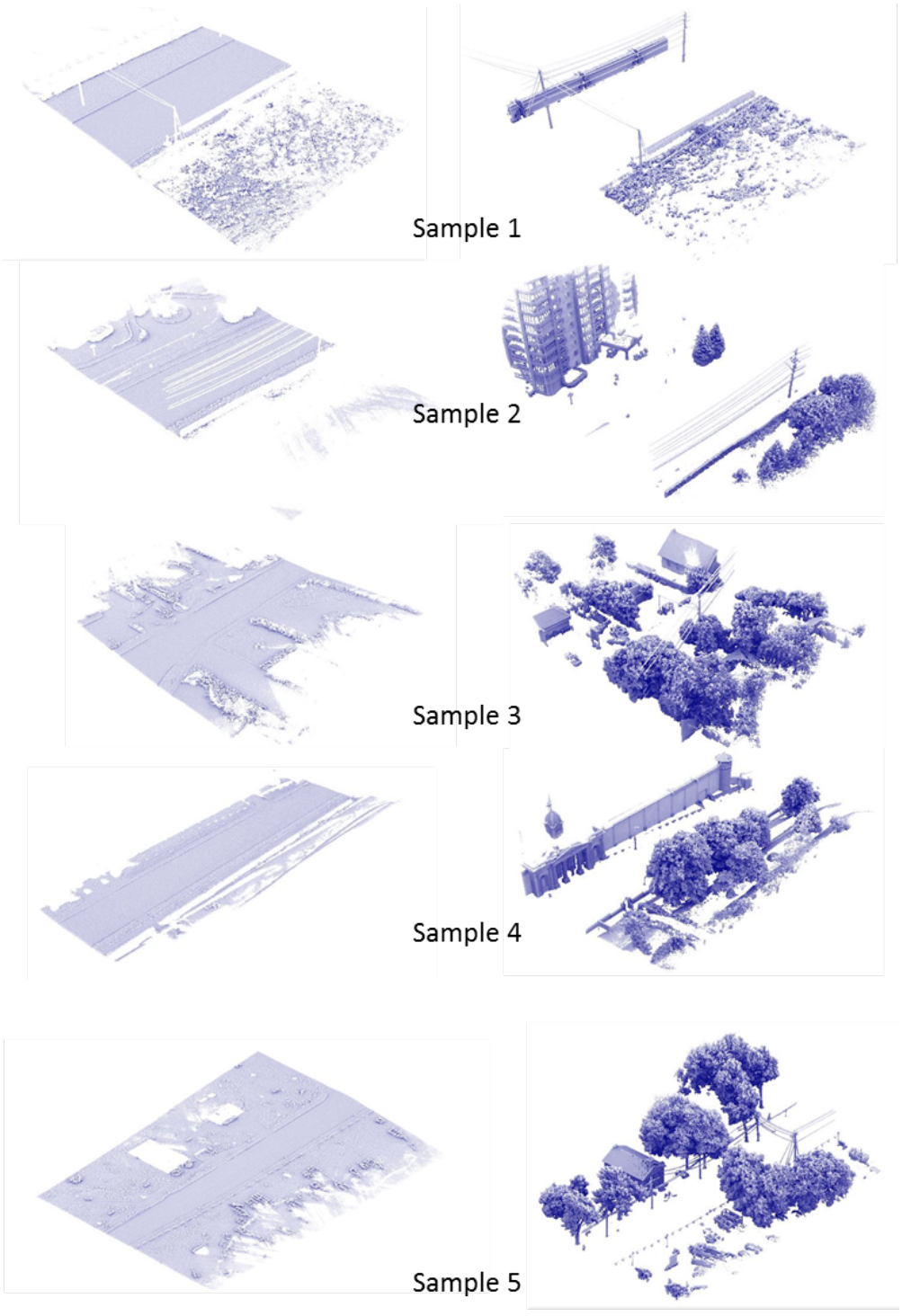

Figure 4.10: Filtering results of five samples. The point clouds were displayed by intensity value.

Table 4.2: Accuracy assessment of five sample sites.

Test Sample	Overall Accuracy	Correctness	Completeness	Type I Error	Type II Error
Sample 1	0.970	0.982	0.982	0.019	0.085
Sample 2	0.984	0.986	0.994	0.006	0.056
Sample 3	0.990	0.991	0.993	0.007	0.015
Sample 4	0.949	0.971	0.952	0.048	0.057
Sample 5	0.989	0.983	0.999	0.001	0.029
Average	0.976	0.983	0.984	0.016	0.048

In the case of Sample 2, the following parameter settings were used: w_B = 3 m, w_V = 0.05 m, H_l= 0.55 m, and H_g = 5.5 m. As a result, the overall accuracy, correctness, and completeness are slightly changed to 0.984, 0.986, and 0.994, respectively, and Types I and II error are 0.006 and 0.056, respectively. Even though there are some variations, there is no significant improvement in this case. The potential reasons of high Type II error rate will be discussed in the next section.

Since Sample 4 has steep slope adjacent to the road surface, this algorithm cannot produce high accuracy and low Type II error at the same time. The final goal is to generate more accurate DTM, instead of perusing high accuracy rate. Thus, it is more reasonable to decrease the Type II error rate. Parameters w_B = 3 m, w_V = 0.05 m, H_l= 0.5 m, and H_g = 5 m were used in the filter. As expected, the overall accuracy, completeness, and Type II error were all dropped down to 0.915, 0.898, and 0.051, and the correctness and Type I error increased to 0.972 and 0.103, respectively. There is the only slight decrease of the Type II error rate, but the cost of decreasing overall accuracy is huge.

Based on the above experimental results, it is can be concluded that the local and global relief terrain heights influence the performance of the proposed algorithm. But they can only slightly improve the accuracy of the filter most of the time. In a typical urban scenario, the global thresholds can be applied in the same dataset. But if the MLS data scenes have much lower vegetation cover such as grassland, the local and global terrain relief heights should be set lower than the global setting. In addition, the scene with high relief terrain feature such as steep slope cannot produce a satisfied result. Decreasing local and global terrain relief heights can help to obtain lower Type II error rate. However, the overall accuracy will also be reduced. A basic understanding of the entire dataset is required to choose an appropriate set of parameters.

4.1.3 Qualitative Analysis of Voxel-based Upward Growing Algorithm

This section analyzes the voxel-based upward growing Algorithm's performance through visual interpretation of the cross matrix image. The cross matrix image is presented in Figure 4.11, which shows where the most errors occur. There are two main types of errors in all these five samples, including terrain with the steep slope and terrain with lower vegetation.

Firstly, steep slope is the most common obstacle for existing filters. In this study, Sample 4 is a scene with the steep slope and steep-sloped vegetation in an urban area. As shown in Figure 4.12, Sample 4 has very steep slope approximately 45° on the left side of the road, and the terrain relief is also relative large along the road's direction. The figure also shows that there are many Type I errors which are in blue colour as the filter falsely detected

the terrain points as off-terrain points.

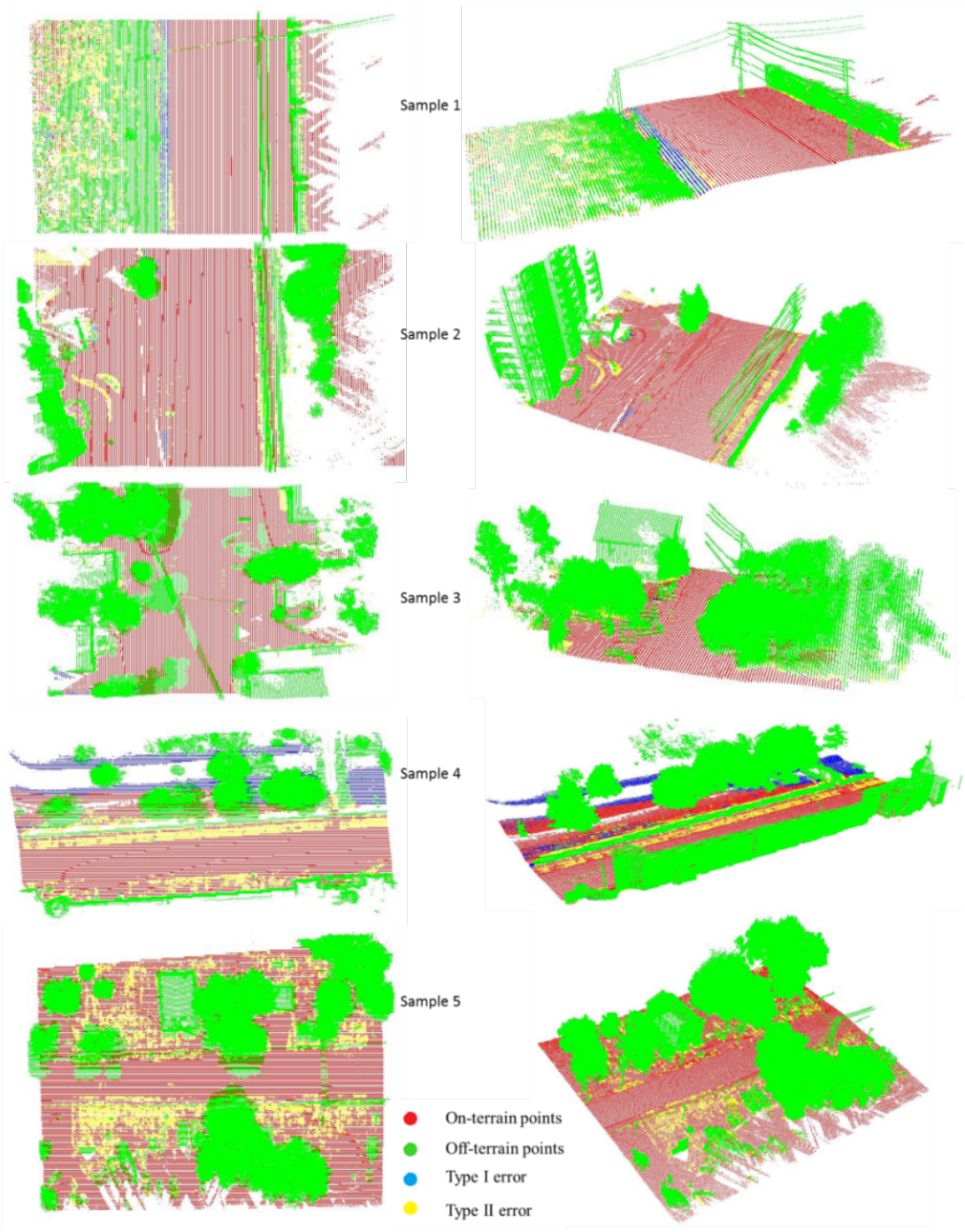

Figure 4.11: Cross matrix image of samples: left side is top view and right side is front view.

Similarly, Sample 1 has same problem with steep slope near 35°. There is a steep slope right beside with the road surface as shown in Figure 4.13 (a). As a result, there is a strip of Type I errors next to the road surface. The main reason is that the algorithm directly filtered the point clouds by setting local and global terrain relief heights. On the other hand, the algorithm is based on the voxel growing up process. Once the voxel is on a steep slope, the terrain voxel cannot stop the growth since it has 9 upper layer neighbours. Thus, the points on the steep slope are misclassified as off-terrain points. If increasing H_l and H_g to reduce the errors, the grow up process will still have the same problem, and objects such as vegetation or building at lower elevation will partially classified into ground category. The algorithm works well for areas with slope along the road direction which is not steep. Therefore, it is difficult to process data well for areas with steep slope by using the proposed filter.

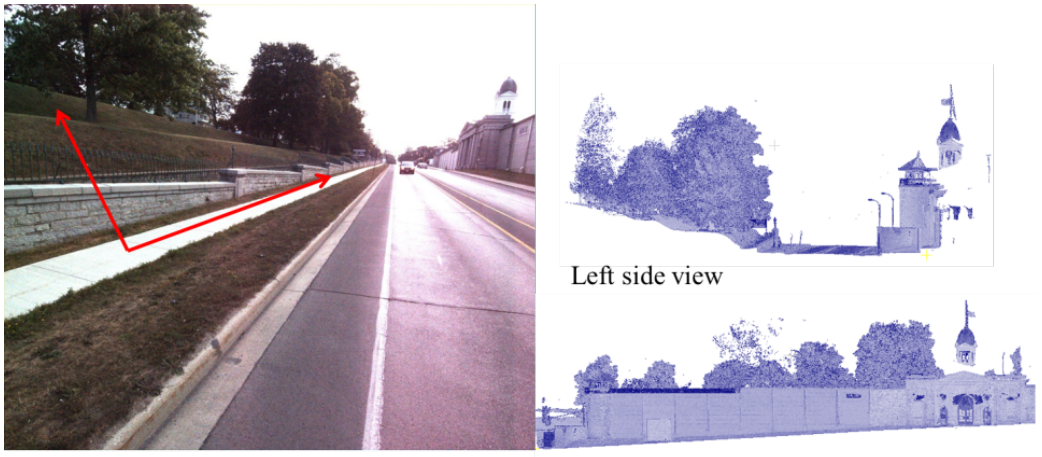

Figure 4.12: Illustration of off-terrain feature for Sample 4

Figure 4.13: Example of areas which are difficult to filter with the proposed method.

Secondly, the short vegetation such as grassland is another main problem of this method. Figure 4.11 shows that Samples 1, 4 and 5 are all contain many Type II errors. Those errors occurred in the short grass (less than 5 cm height) areas as shown in Figure 4.13 (b) and (c). When samples are labeled by visual interpretation, human brain can make assumption if it is short-grass or terrain point by cross comparison of the point clouds with digital photos. However, the proposed filter algorithm is not as intelligent as human brain. Thus, many points which are short grass were identified as terrain points. In most cases, Type II error can be ignored since the short vegetation is less than 5 cm height.

Even though there are some errors produced by the proposed filter, the overall performance of this algorithm is quite satisfied. Section 2.3 states that some previous study had difficulties in processing objects with different sizes in one scene such as huge buildings, small buildings, and vehicles. Figure 4.14 illustrates that the large and small buildings, vehicles on the ground, short walls, and even pedestrians can be filtered out in some cases in one scene with excellent performance. It is confident that this algorithm is suitable for most situations no matter if it is urban or non-urban area except areas with steep slopes.

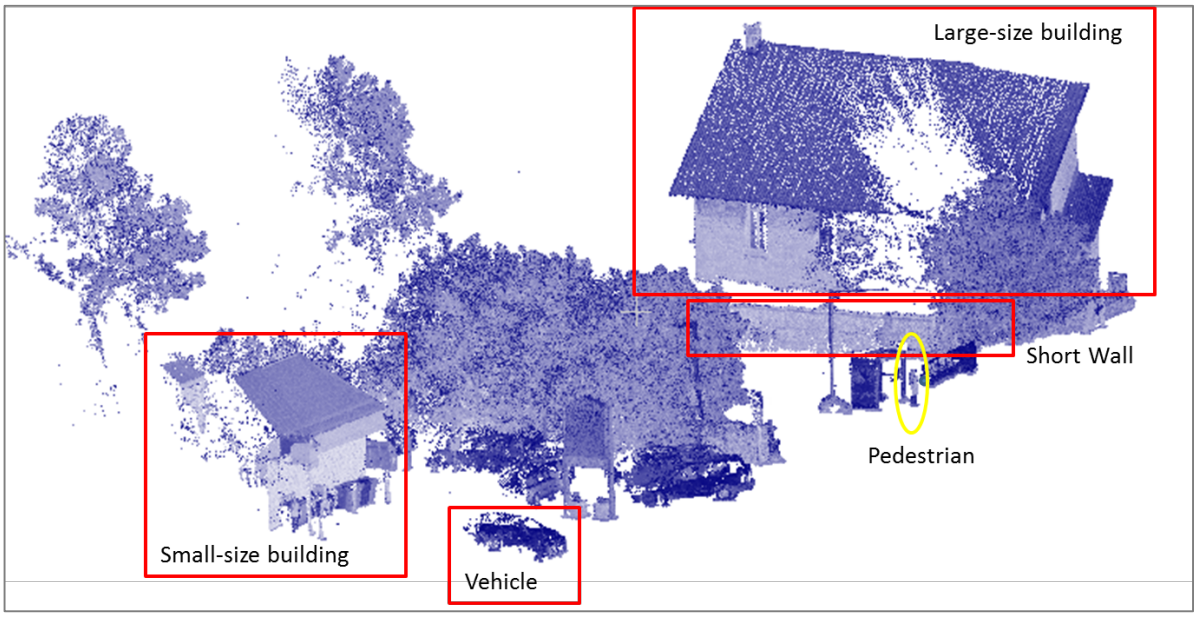

Figure 4.14: Off-terrain points detection from a complex point cloud scene.

4.2 Generation of Gridded DTMs

The final gridded DTM of the study is a DTM database which includes DTMs with various cell sizes, i.e. 2cm, 5 cm, 10cm, 15 cm, 20 cm, 25 cm, 30cm, 35 cm, 40 cm, 45 cm, 50 cm, and 1m. In order to present the DTM that covers the entire study area well, the DTM was clipped into three parts. Parts 1, 2, and 3 were snapped starting from east side to west side of the study area. Figure 4.15 illustrates the DTM interpolated by the IDW interpolation method with 5 cm grid size. The elevation of the entire study area ranges from 73.28 m to 97.20 m.

As shown in Figure 4.15, there is no obvious terrain changes between road and non-road areas in Parts 1 and 2 which are located near the centre of the city. However, there are more differences between the road and non-road areas in Part 3 of DTM. The satellite image, see Figure 3.2 (b), shows the Part 3 area is out of city centre, and the surveyed road crosses a

bay of Lake Ontario that results in larger terrain relief between the road and non-road area.

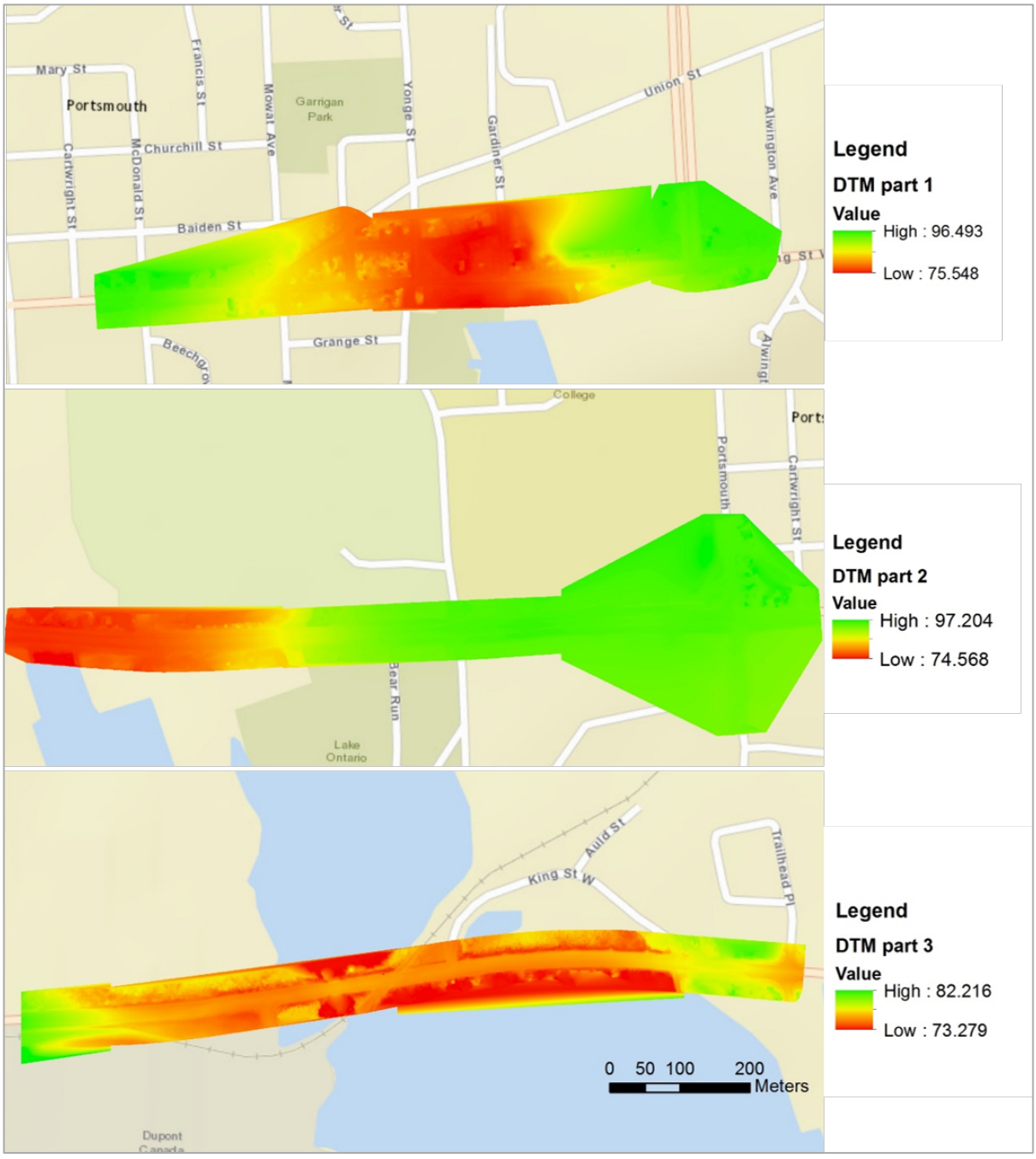

Figure 4.15: DTMs of the study area which interpolated by IDW with 5 cm grid size.

4.3 Quality of Gridded DTMs

One of the main objectives of this study is to examine the accuracy of DTMs generation using MLS data. Thus, the final accuracy assessment of DTMs is very important. This section states and discusses the accuracy analysis of the final gridded DTM. It includes internal and external accuracy assessments. The performance of different interpolation methods is also discussed. In addition, the accuracy of DTMs generated from different dense point clouds is compared.

4.3.1 Internal Accuracy Assessment of Gridded DTMs

Since the GPS check points have large difference from the MLS dataset, 200 ground points from MLS point clouds were randomly chosen to use in internal validations of the vertical accuracy in this study. This greatly reduces the influences of random errors occurred during the process of evaluating the suitability of interpolation method used in MLS point clouds. In addition, various grid sizes of DTMs were generated. Since the objective of this research is to generate high-accuracy and high-resolution DTMs, 12 grid sizes were used, i.e. 2 cm, 5 cm, 10 cm, 15 cm, 20 cm, 25 cm, 30 cm, 35 cm, 40 cm, 45 cm, 50 cm, and 1 m. Then the RMSE, absolute mean error, standard deviation, and standard error were calculated by equations listed in Section 3.6.2 to examine the relationship between the DTMs generated by four different interpolation methods and check points.

4.3.1.1 Accuracy Assessment of Different Interpolation Methods and Grid Sizes

The internal accuracy assessment of different interpolation methods is shown in Figure 4.16. The overall trend of these four interpolation results was with the increasing grid size, the accuracy of interpolated DTM decreases. All RMSEs of these results were less than

3.5 cm, and all absolute mean errors ranged between 0.3 and 2 cm. Each interpolation method has its own trend. For the IDW interpolation, there was a gentle growth of errors with increased grid size. But after the grid size increased to 35 cm, the growth rate of errors rapidly increased.

Different from the IDW interpolation, the Nearest Neighbour interpolation started with relative large RMSE and absolute mean error, i.e. 1.12 cm and 0.41 cm, respectively. All the accuracy results of DTMs were almost the same for resolution less than 20 cm and then followed by an increasing trend of errors. The Linear interpolation and Natural Neighbours interpolation have a similar trend which increases with fluctuations when grid size increases. Compared to the Natural Neighbours method, the Linear interpolation has the lowest RMSE value at 2 cm resolution, i.e. 0.63 cm. In summary, the IDW and Nearest Neighbour have more stable performance than Linear and Natural Neighbours interpolation for different grid sizes.

In order to explore the relationship between these four interpolation methods and grid size setting, four line charts were generated, as illustrated in Figure 4.17. The standard deviation increases as the grid size increase for all four interpolation methods. Not only the RMSE tends to become larger with increasing grid size, but the variations of those errors increase too. The RMSE, standard deviation, and standard error have similar trends. The absolute mean error of these four interpolation methods ranges from 0.3 cm to 1.93 cm.

As Figure 4.17 shows, the IDW has the highest accuracy among four interpolation methods with most grid sizes. When setting the grid size to 2cm, results generated by IDW

and Linear interpolations have excellent quality (less than 1 cm) with all statistical indices. In addition, all IDW interpolation with grid size less than 20 cm results in RMSE of less than 1 cm. However, once the grid size increased to 1 m, IDW is no longer the best interpolation method. All four statistical values were greater than Linear and Natural Neighbours interpolation. For example, the RMSE of IDW and Linear interpolation with 1 m grid size were 3.08 cm and 2.83 cm, respectively. Therefore, from the perspective of accuracy, IDW interpolation is more suitable to interpolate terrain MLS point clouds when generating high-resolution (grid size smaller than 1 m) gridded DTMs.

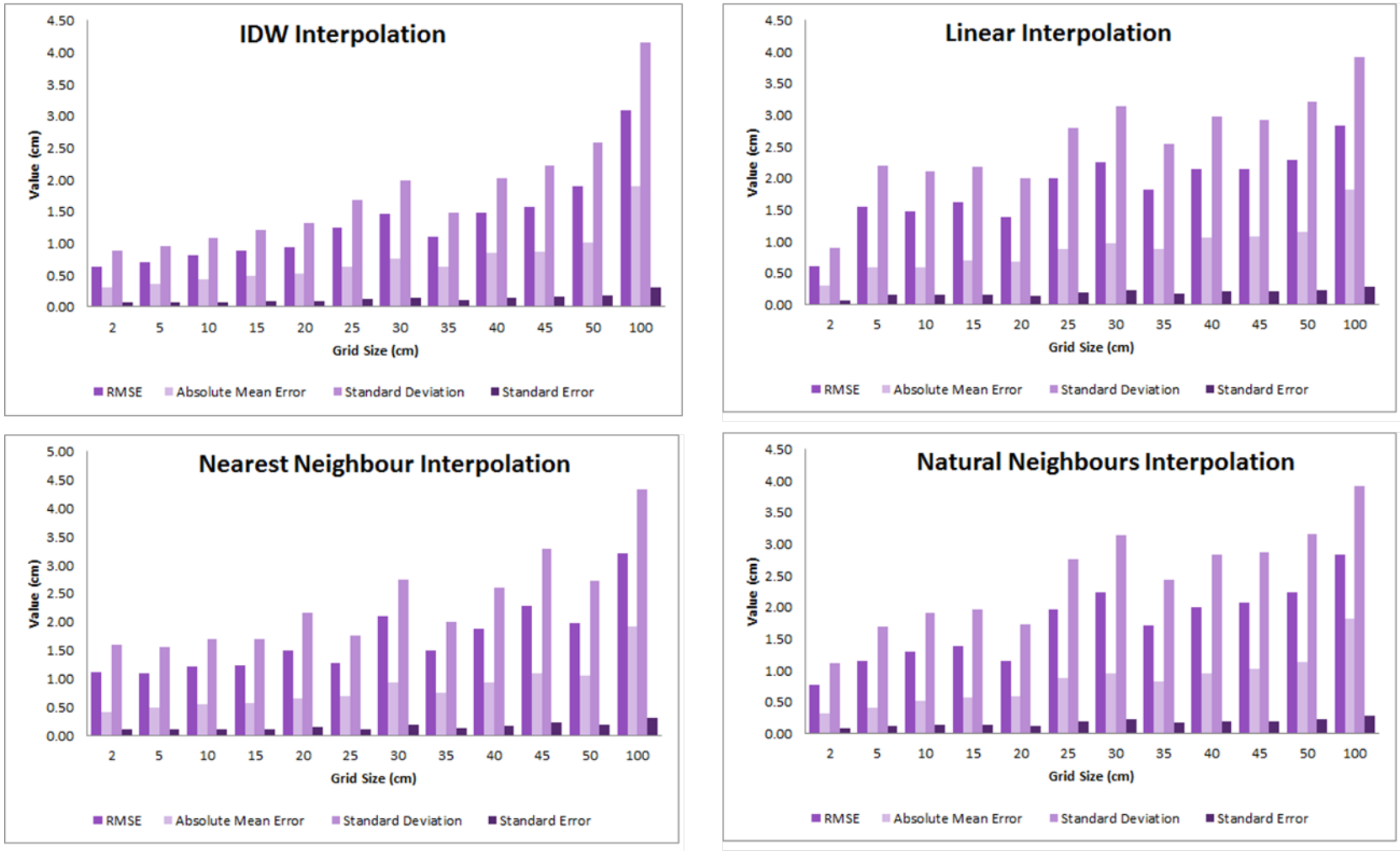

Figure 4.16: Internal accuracy assessment results.

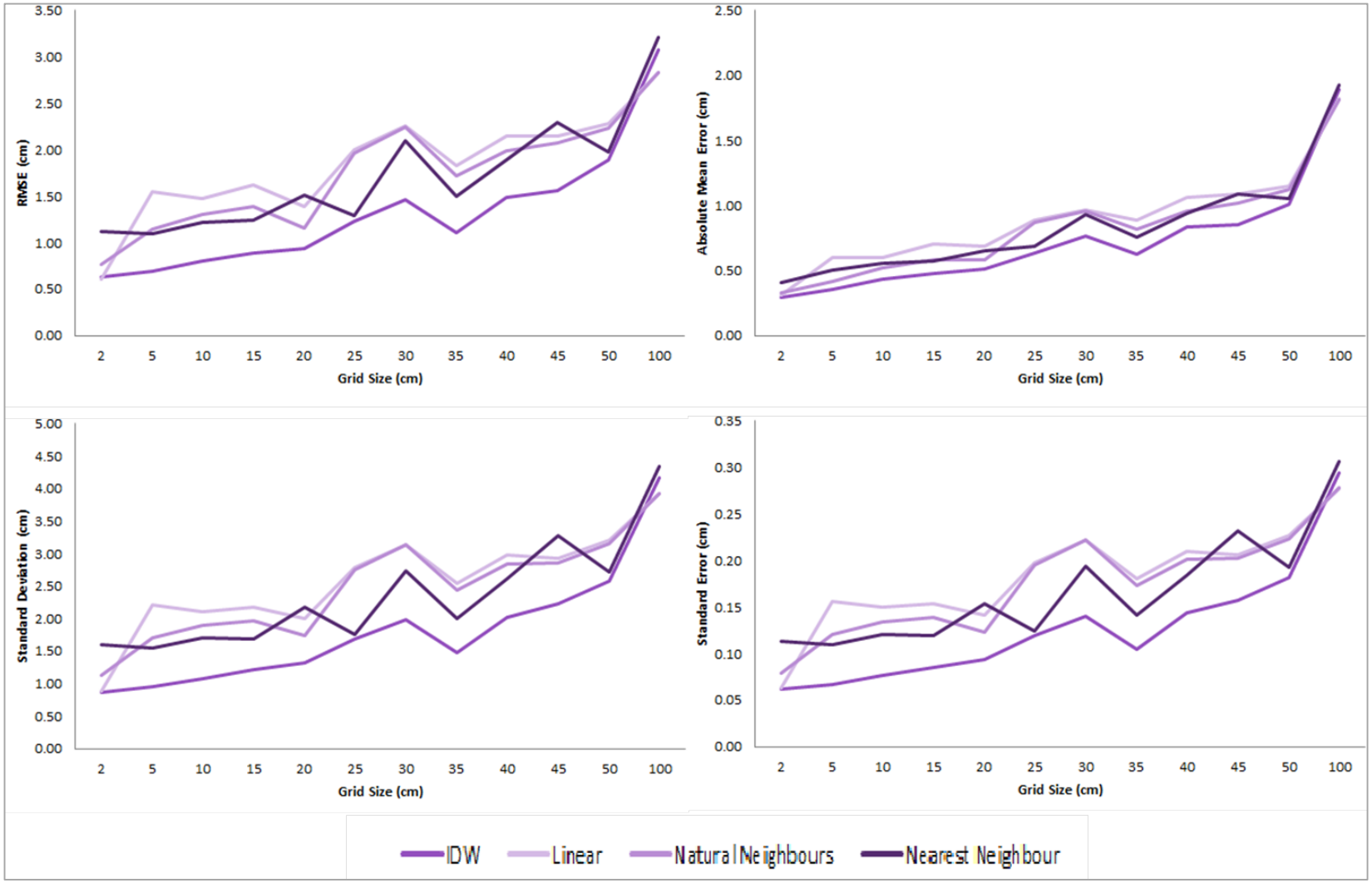

Figure 4.17: Internal RMSE, absolute mean error, standard deviation, and standard error of different grid sizes for four interpolation methods.

4.3.1.2 Computational time of Different Interpolation Methods and Grid Sizes

Computational time is another vital factor when determining a suitable interpolation method of the MLS point clouds. Figure 4.18 shows that the computational times of all four interpolations were similar with increasing grid size. There were rapid reductions in computing time between 2 cm to 5 cm size of the grid. With increasing grid size, the computational time becomes constant. When the grid size was set to 2 cm, the calculation speed of these four interpolations was very slow. But the Natural Neighbours interpolation was the most time-consuming algorithm. The reason is that the average spacing between points is between 2 cm and 1 cm for this dataset, as indicated by Table 3.1. Thus, the interpolation process requires more time to compute and assign values to the 2 cm-grid DTM. If the grid size is larger than the average spacing, it saves more time to process the interpolation.

The IDW and Nearest Neighbour algorithms have almost the same trend for the computational time. The Linear and Natural Neighbours interpolations need triangulation first, which result in more computational time. The Linear interpolation has a sudden increase of computing time at 35 cm grid size, which is related to the accuracy. As shown in Figure 4.16, 35 cm grid size has higher accuracy compared to grid sizes of 30 cm and 40 cm. As a result, the computational time is higher too. To summarise, IDW and Nearest Neighbour interpolations have better computational performance when generating gridded DTMs from MLS point clouds.

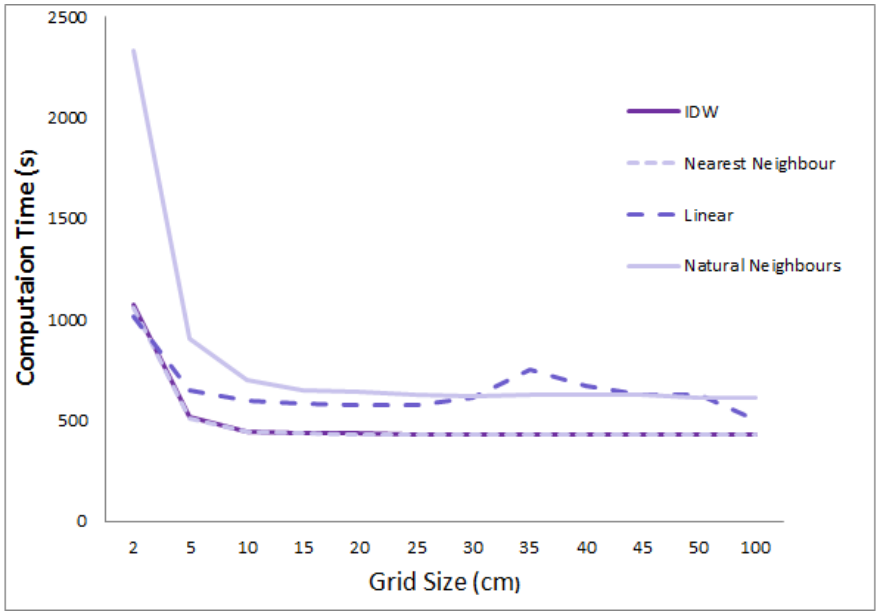

Figure 4.18: Computational time of four interpolation methods with different grid sizes.

4.3.1.3 Accuracy of DTMs Generated with Different Dense MLS Point Clouds and Grid Sizes

In order to discover whether the density of MLS point clouds affects the accuracy of DTMs, a comparison experiment was conducted. It compares the RMSEs of DTM using different dense point clouds of Sample 3, and the results are presented in Figure 4.19. Based on the GPS time stored in the MLS dataset, three types of various density point clouds were extracted from the original Sample 3 which was surveyed five times, i.e. once measured point clouds (one direction observation), twice measured point clouds (bi-direction observation), and four-time measured point clouds (twice bi-direction observations). The IDW was applied to all these three different dense point clouds and the original point cloud for DTMs generation due to its good performance.

Figure 4.19 shows the RMSE of DTMs generated from these four various dense point clouds. Results demonstrate that the RMSEs had no significant difference when the grid size

is larger than 25 cm. However, if the grid size is smaller than 25 cm, the density of MLS point clouds could impact the final accuracy of DTM. When the grid resolution is smaller than 10 cm, more dense point clouds can produce more accurate DTMs. Four-time and five-time measured data provide similar accuracy when generating DTMs. The RMSEs of DTMs at 2 cm resolution were 0.6 cm for four-time measurements and 0.63 cm for five-time measurements. The RMSEs of once measurement and twice measurement were 0.91 cm and 0.75 cm, respectively. It is clear that using five-time measured point clouds to generate high-resolution DTM can almost double the accuracy than using once measured MLS data. When the grid size was between 10 cm to 25 cm, the DTMs accuracy of once and twice measured point clouds tended to be the same. The four-time and five-time measured point clouds tended to produce the DTMs with similar accuracy.

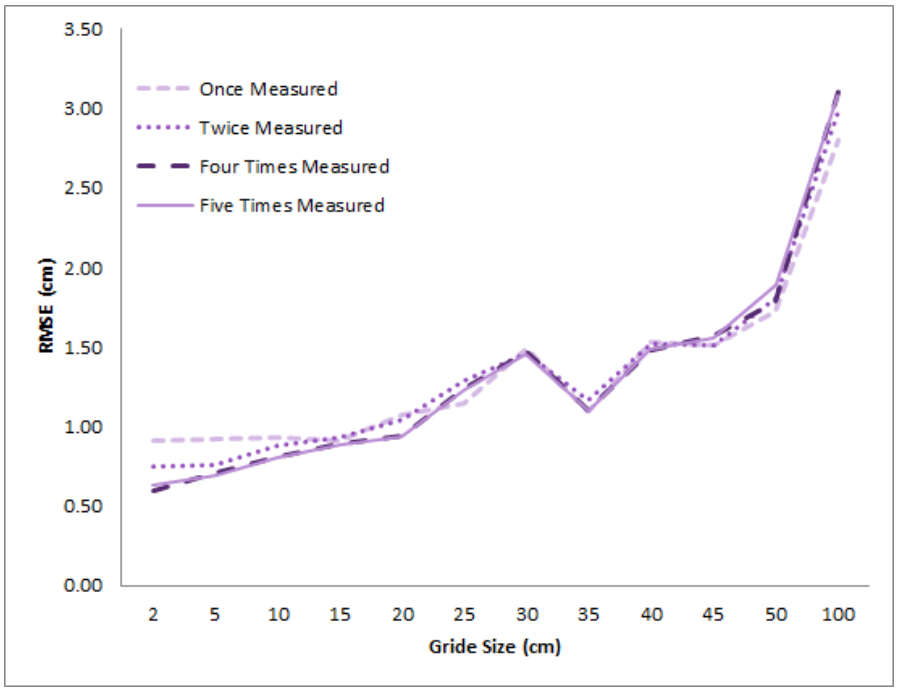

Figure 4.19: RMSE of DTMs using different dense point clouds with different grid sizes.

In summary, when the grid size of DTM is smaller than 25 cm, the more dense point clouds can produce more accurate results. MLS point clouds with average spacing around 1-2 cm and point density greater than 4000 points/m^2 can provide satisfactory results of interpolation. If the DTM grid size is greater than 25 cm, the point clouds with 1000 to 5000 points/m^2 have similar accuracy in gridded DTMs generation.

4.3.2 External Accuracy Assessment of Gridded DTMs

Through calculation of a series of statistical measures which are described in Section 3.6.2, the final absolute accuracy of gridded DTMs was obtained. The final results of external accuracy assessment are presented in Figures 4.20 and 4.21, and Table 4.3.

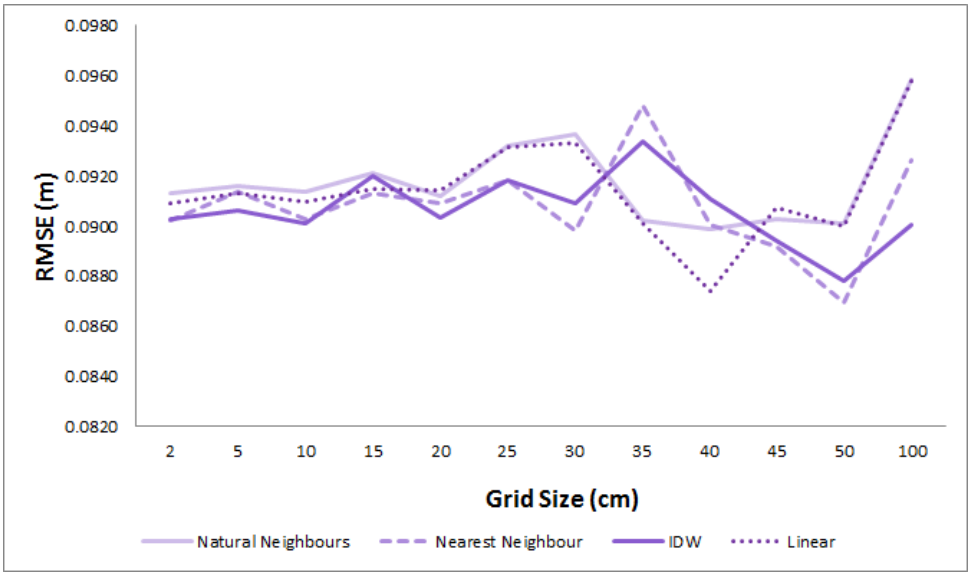

Figure 4.20: External accuracy assessment of RMSE with different interpolation methods and grid sizes.

Figures 4.20 and 4.21 show some distribution of the external assessment in terms of RMSE and absolute mean error. Similar to the trend of internal accuracy assessment, the external accuracy has a gentle growth as the grid size of DTM increases with fluctuations.

The accuracies of each interpolation methods were compared to each other with no more than 1.1 cm in RMSE and 0.7 cm in absolute mean error. It means that there is no large difference between four interpolation methods in terms of external accuracy. Since the external check points were surveyed by GPSs, which contain some random errors, the accuracy of DTMs shows more fluctuations than the internal accuracy assessment results.

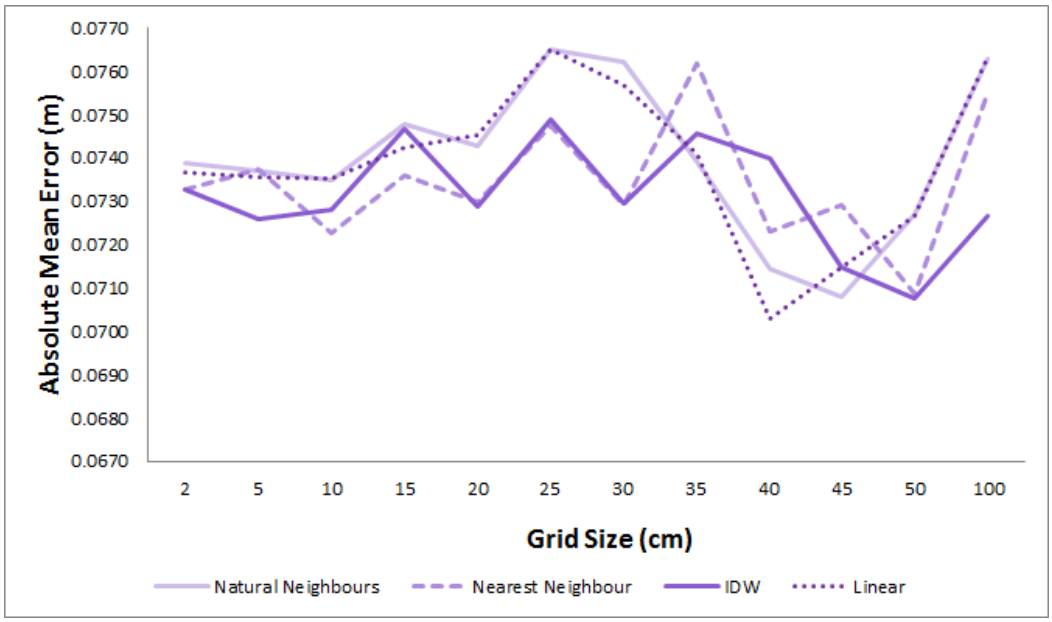

Figure 4.21: External accuracy assessment of absolute mean error with different interpolation methods and grid sizes.

Figures 4.20 and 4.21 show a significant drop of RMSE and absolute mean error for grid sizes between 30 cm and 50 cm. It indicates that the accuracy of cell sizes between 30 cm and 50 cm is higher than other grid sizes. However, neither the RMSE nor the absolute mean error had a deviation greater than 1 cm. This may be caused by the locations of check points. Some of the 30 randomly selected check points are probably located near the centers of 30 to 50 cm grids. Another reason could be the random errors of check points. But

according to the internal accuracy assessment, the 35 cm grid size DTM obtained higher accuracy than others which is consistent with external accuracy. Based on these results, grid size should be set at 35 cm when interpolating MLS points.

Table 4.3 contains the entire external accuracy of DTMs generated in different cell sizes. The standard deviations of RMSE range from 13.5 to 15.5 cm. According to Congalton and Green (2008), a confidence interval around the RMSE at 95% probability range and the interval of errors around RMSE which includes 95% of map errors range were calculated. As shown in Table 4.3, the confidence interval around the RMSE at 95% probability range distributed from 3.7 cm to 15.1 cm. It means all grid-sized DTMs have 95% confidence to present that the RMSEs are in this range. The interval of errors around RMSE which includes 95% of map errors range was settled between -20 cm and 40 cm. In addition, Table 4.3 shows that the RMSEs were all ranged between 8.5 cm and 9.6 cm. The absolute mean errors were in the range of 7 cm - 7.7 cm.

The ALS-derived metre-level resolution DTM usually has 20 cm accuracy in RMSE (Bater and Coops, 2009; Veneziano et al., 2002). However, MLS-derived DTMs with grid size smaller than 1 m can provide the absolute accuracy of RMSE at 10 cm level. The RMSEs are distributed from 3.7 cm to 15.1 cm with 95% confidence. In addition, the DTMs with smaller than 1 m grid size have similar absolute accuracies which are ranged in 1.1cm of RMSE. To obtain the best interests with MLS point clouds, the cell size of DTM should be set as 30-40 cm.

Table 4.3: External accuracy assessment.

Interpolation	Grid Size(cm)	Mean Error (cm)	Absolute Mean Error (cm)	RMSE (cm)	Standard Deviation (cm)	Standard Error (cm)	A confidence interval around the estimate of RMSE at 95% probability range (cm)		The interval of errors around RMSE which includes 95% of map errors range (cm)	
IDW	2	-2.16	7.33	9.03	14.45	2.64	3.85	14.20	-19.31	37.36
IDW	5	-2.26	7.26	9.06	14.56	2.66	3.85	14.27	-19.49	37.60
IDW	10	-2.12	7.28	9.01	14.40	2.63	3.86	14.16	-19.22	37.24
IDW	15	-2.30	7.47	9.20	14.80	2.70	3.91	14.50	-19.80	38.20
IDW	20	-2.11	7.29	9.03	14.43	2.63	3.87	14.20	-19.25	37.31
IDW	25	-2.16	7.49	9.18	14.68	2.68	3.93	14.43	-19.58	37.95
IDW	30	-2.37	7.30	9.09	14.68	2.68	3.84	14.34	-19.69	37.87
IDW	35	-2.43	7.46	9.33	15.07	2.75	3.94	14.73	-20.21	38.88
IDW	40	-2.58	7.40	9.11	14.84	2.71	3.80	14.42	-19.98	38.19
IDW	45	-2.33	7.15	8.94	14.44	2.64	3.77	14.11	-19.36	37.24
IDW	50	-2.07	7.08	8.78	14.04	2.56	3.76	13.80	-18.74	36.30
IDW	100	-1.29	7.27	9.00	13.85	2.53	4.05	13.96	-18.14	36.15
Linear	2	-2.32	7.37	9.09	14.65	2.68	3.85	14.33	-19.63	37.81
Linear	5	-2.25	7.36	9.13	14.66	2.68	3.88	14.38	-19.61	37.87
Linear	10	-2.27	7.35	9.09	14.62	2.67	3.86	14.32	-19.56	37.75
Linear	15	-2.12	7.43	9.15	14.61	2.67	3.92	14.38	-19.48	37.78
Linear	20	-2.17	7.45	9.14	14.63	2.67	3.91	14.37	-19.53	37.81
Linear	25	-2.56	7.65	9.32	15.13	2.76	3.90	14.73	-20.34	38.97
Linear	30	-2.24	7.57	9.33	14.95	2.73	3.98	14.68	-19.96	38.62
Linear	35	-1.83	7.41	9.01	14.22	2.60	3.92	14.10	-18.85	36.88
Linear	40	-1.59	7.03	8.74	13.67	2.49	3.85	13.63	-18.05	35.52
Linear	45	-2.48	7.15	9.07	14.73	2.69	3.80	14.34	-19.79	37.94
Linear	50	-2.03	7.27	9.00	14.33	2.62	3.87	14.13	-19.09	37.08
Linear	100	-2.41	7.63	9.58	15.41	2.81	4.06	15.10	-20.63	39.79

Interpolation	Grid Size(cm)	Mean Error (cm)	Absolute Mean Error (cm)	RMSE (cm)	Standard Deviation (cm)	Standard Error (cm)	A confidence interval around the estimate of RMSE at 95% probability range (cm)		The interval of errors around RMSE which includes 95% of map errors range (cm)	
Natural Neighbours	2	-2.32	7.39	9.13	14.71	2.69	3.87	14.39	-19.70	37.95
Natural Neighbours	5	-2.30	7.37	9.16	14.73	2.69	3.89	14.43	-19.71	38.03
Natural Neighbours	10	-2.27	7.35	9.14	14.68	2.68	3.88	14.39	-19.64	37.91
Natural Neighbours	15	-2.17	7.48	9.21	14.72	2.69	3.94	14.47	-19.64	38.06
Natural Neighbours	20	-2.19	7.43	9.12	14.61	2.67	3.89	14.35	-19.51	37.75
Natural Neighbours	25	-2.55	7.65	9.32	15.13	2.76	3.91	14.74	-20.34	38.98
Natural Neighbours	30	-2.28	7.62	9.36	15.02	2.74	3.99	14.74	-20.07	38.80
Natural Neighbours	35	-1.90	7.39	9.02	14.27	2.61	3.91	14.13	-18.96	36.99
Natural Neighbours	40	-2.09	7.14	8.98	14.35	2.62	3.85	14.12	-19.13	37.10
Natural Neighbours	45	-2.49	7.08	9.03	14.67	2.68	3.78	14.28	-19.72	37.78
Natural Neighbours	50	-2.06	7.27	9.01	14.36	2.62	3.87	14.15	-19.14	37.16
Natural Neighbours	100	-2.41	7.63	9.58	15.42	2.82	4.07	15.10	-20.64	39.81
Nearest Neighbour	2	-2.12	7.33	9.02	14.41	2.63	3.86	14.18	-19.23	37.27
Nearest Neighbour	5	-2.20	7.37	9.14	14.64	2.67	3.90	14.37	-19.55	37.83
Nearest Neighbour	10	-1.96	7.23	9.02	14.32	2.61	3.90	14.15	-19.05	37.10
Nearest Neighbour	15	-2.13	7.36	9.13	14.59	2.66	3.91	14.35	-19.46	37.72
Nearest Neighbour	20	-2.09	7.30	9.09	14.50	2.65	3.90	14.28	-19.32	37.50
Nearest Neighbour	25	-2.16	7.48	9.18	14.68	2.68	3.93	14.44	-19.59	37.96
Nearest Neighbour	30	-1.99	7.29	8.98	14.28	2.61	3.87	14.09	-19.01	36.97
Nearest Neighbour	35	-2.33	7.62	9.48	15.22	2.78	4.04	14.93	-20.35	39.32
Nearest Neighbour	40	-2.25	7.23	9.00	14.48	2.64	3.82	14.18	-19.37	37.37
Nearest Neighbour	45	-2.30	7.29	8.92	14.38	2.63	3.77	14.06	-19.28	37.11
Nearest Neighbour	50	-2.04	7.09	8.69	13.89	2.54	3.72	13.67	-18.54	35.93
Nearest Neighbour	100	-1.30	7.55	9.26	14.23	2.60	4.17	14.35	-18.62	37.14

4.4 Chapter Summary

In this chapter, the DTMs generated from MLS point clouds are presented. The parameters of voxel-based upward growing algorithm were analyzed. Meanwhile, the quantitative and qualitative analysis demonstrated that the voxel-based upward growing filter obtained excellent results with average overall accuracy of 0.975. However, when processing terrain with steep slope, the performance of the proposed algorithm was not satisfactory. Finally, the gridded DTMs were evaluated both in internal and external examinations. The results showed that the IDW interpolation is more suitable for interpolating ground points into raster DTMs due to higher accuracy and shorter computational time. The final delivered DTM can reach 10 cm absolute accuracy under 1 m grid size.

Chapter 5
Conclusions and Recommendations

This chapter presents the conclusions of this study, describes its limitations, and proposes some suggestions for future studies.

5.1 Conclusions

One of the best features of MLS is that it can collect high density point clouds, which are also its biggest drawbacks in terms of processing these large volumes of data. Thus, this research has focused on how to efficiently and accurately apply the MLS point clouds to generate DTMs along roads. The proposed workflow provides a satisfactory approach, and objectives proposed have been fulfilled.

A semi-automated voxel-based upward growing algorithm has been applied to classify the terrain points from raw MLS point clouds. To reduce the processing time, this algorithm first decomposes a large scene of point clouds into a set of blocks, and partitions each block into voxels. Then an upward growing process is employed to determine whether a voxel belongs to terrain or off-terrain. Four parameters of this algorithm were defined and analyzed separately for sensitivity analysis. The voxel-based upward growing algorithm was evaluated quantitatively and qualitatively. The results obtained using a set of global thresholds of five selected datasets show that the algorithm was able to achieve the average overall accuracy, correctness, and completeness values of 0.975, 0.98, and 0.986, respectively. In some cases, the overall accuracy was more than 0.990. The average rates of Types I and II errors were 0.014 and 0.064, respectively. By visual inspection of the cross matrix images, it can be seen that the voxel-based upward growing algorithm performed well

except for those areas with steep slopes. This finding indicates that this algorithm is more suitable for areas without steep slopes.

In this study, four types of interpolation methods, namely IDW, Nearest Neighbour, Linear, and Natural Neighbour, were used to interpolate ground points for obtaining gridded DTMs. Internal and external accuracy assessments were carried out. Under a grid size setting of less than 1 m, IDW has proven to be the best method for interpolating ground points into raster DTMs, due to its superior accuracy and computation process speed. When the grid size of DTMs is smaller than 25 cm, accuracy grows higher as the density of the clouds increases. When the cell size is large than 25 cm, the point clouds that have 1000 to 5000 points/m² provides similarly accurate DTMs. In terms of absolute accuracy of DTMs, the external accuracy illustrated that the final products of all cell-size DTMs with 2 cm to 1 m can provide a 10 cm-level (RMSE) accuracy DTM.

In conclusion, MLS is an effective system in obtaining DTMs. The proposed methodology has proven to be successful in generating DTMs with high-accuracy and high-resolution from MLS point clouds. DTMs with centimetre resolution and 10 cm accuracy can be obtained from MLS data. Even though the final gridded DTMs do not meet the engineering survey level (less than 5 cm of vertical accuracy) required by transportation agencies, they are still useful for other transportation applications, including road features extraction, autonomous navigation, roadway condition assessment, and selected hydrological modeling on road surfaces. MLS technology can be an efficient and safe approach for operations all along roads to generate DTMs.

5.2 Limitations and Recommendations

In this study, the proposed methodology in generating DTMs from MLS point clouds has provided a satisfactory result in this paper. However, certain limitations are noted below.

Firstly, while the proposed filter has produced favourable results in most scenes including typical urban areas and non-urban areas. This algorithm does not work in areas with steep slopes. This is because that the algorithm is based on upward growing processes. Voxels located on steep slopes cannot grow up as well as on flat areas. Therefore, for steep terrain areas, the algorithm will need to be revised and improved. Secondly, setting appropriate parameters is another limitation which reduces the automation of this filter. According to this filter, it is necessary to have prior knowledge, in setting heights of the dataset for the local and global terrain relief. While a global threshold set could be applied into one dataset, in order to obtain more accurate filtering results, the parameters used in different tiles of datasets may need adjusting accordingly. The adjustment of these parameters requires more manual interactions. Therefore, an automatic generation of the parameters could be developed in the future. The parameters used in the proposed filter may be automatically set by methods such as artificial intelligence.

Moreover, due to limitation in the data availability, this study only proves that the proposed filter algorithm is not suitable in steep slope areas. However, the details of how well the algorithm works at steeper slopes are not discussed. Thus, in the future, should there be more available datasets for different degrees of slope; the algorithm may be tested again. The applicability of the algorithm would then be known better.

Furthermore, the final DTM products with an absolute accuracy of 10 cm are not sufficient compared to the required absolute accuracy of 2-5cm set by transportation agencies. However, a more accurate DTM product can be achieved in the future by improving the accuracy of DTMs, some approaches can be used in the future to improve the accuracy of measurements of the MLS system. For example, calibration targets can be used during MLS system measurement period to improve the accuracy of MLS raw data.

Lastly, the proposed algorithm was originally designed for MLS point clouds. Considering the similarity between TLS data and MLS data, it may be possible to also apply this voxel-based upward growing method into TLS point clouds. Therefore, in the future, more experiments can be conducted in evaluating whether this algorithm may be applicable when working with terrestrial laser-scanned data.

References

Abellan, A., Jaboyedoff, M., Oppikofer, T., and Vilaplana, J. M. (2009). Detection of millimetric deformation using a terrestrial laser scanner: experiment and application to a rockfall event, *Natural Hazards and Earth System Sciences*, 9: 365–372.

Akel, N. A. and Zilberstein, O. (2004). A robust method used with orthogonal polynomials and road network for automatic terrain surface extraction from Lidar data in urban area, *ISPRS Archives*, *35*(B3): 274-279.

Akel, N. A., Kremeike, K. and Filin, S. (2005). Dense DTM generalization aided by roads extracted from Lidar data. *ISPRS Archives*, *36* (3/W19): 54-59.

ArcGIS, ESRI. (2008). 9.2 Desktop help. *ESRI, Redlands, CA*. Retrieved from: http://webhelp.esri.com/arcgisdesktop/9.2/index.cfm?TopicName=welcome

Axelsson, P. (2000). DEM generation from laser scanner data using adaptive TIN models. *ISPRS Archives*, *33*(4): 111-118.

Barber, D., Holland, D., and Mills, J. (2008). Change detection for topographic mapping using three-dimensional data structures. *ISPRS Archives*, *37*(B4): 1177–1182.

Barber, D., Mills, J., and Smith-Voysey, S. (2008). Geometric validation of a ground-based mobile laser scanning system, *ISPRS Journal of Photogrammetry and Remote Sensing*, 63: 128-141.

Bater, C. W., and Coops, N. C. (2009). Evaluating error associated with lidar-derived DEM interpolation. *Computers and Geosciences*, *35*(2): 289-300.

Beraldin, J., Blais, F., and Lohr, U. (2010). Laser scanning technology. In: Vosselman, G. and Mass, H. (eds.), *Airborne and Terrestrial Laser Scanning*, 1-42. Caithness,

Scotland: Whittles Publishing.

Berg, R., and Ferguson, J. (2001). Airborne laser mapping for highway engineering applications. *In Proceedings of the ASPRS Annual Convention*, St. Louis, USA. CDROM

Brus, D. J., Gruijter, J. J., Marsman, B. A., Visschers, B. A., Bregt, A. K., Breeuwsma, A. (1996). The performance of spatial interpolation methods and choropleth maps to estimate properties at points: a soil survey case study. *Environmetrics,* 7: 1-16.

Burrough, P.A., and McDonnell, R.A. (1998). *Principles of Geographical Information Systems*. Oxford: Oxford University Press.

Toutin, T. (2006). Generation of DSMs from SPOT-5 in-track HRS and across-track HRG stereo data using spatio triangulation and autocalibration. *ISPRS Journal of Photogrammetry and Remote Sensing*, *60*(3), 170-181.

Clarke, K. C. (1990). *Analytical and Computer Cartography* (Vol. 290). Englewood Cliffs, NJ: Prentice Hall.

Congalton, R. G., and Green, K. (2008). *Assessing the Accuracy of Remotely Sensed Data: Principles and Practices*. Boca Raton, FL: CRC Press.

Corsini, A., Borgatti, L., Cervi, F., Dahne, A., Ronchetti, F., and Sterzai, P. (2009). Estimating mass-wasting processes in active earth slides - earth flows with time-series of high-resolution DEMs from photogrammetry and airborne LiDAR, *Natural Hazards and Earth System Sciences*, 9: 433–439.

Crosetto, M., (2002). Calibration and validation of SAR interferometry for DEM generation. *ISPRS Journal of Photogrammetry and Remote Sensing,* 57: 213– 227.

Elmqvist, M. (2001). Ground surface estimation from airborne laser scanner data using active

shape models. *ISPRS Archives*, *34*(3/A): 114-118.

Elseberg, J., Borrmann, D., and Nuchter, A. (2013). One billion points in the cloud—An octree for efficient processing of 3D laser scans. *ISPRS Journal of Photogrammetry and Remote Sensing*, 76: 76–88.

El-Sheimy, N., Valeo, C., and Habib, A. (2005). *Digital Terrain Modeling: Acquisition, Manipulation, and Applications*. Norwood, MA.: Artech House.

Fellendorf, M. (2013). Digital terrain models for road design and traffic simulation, *Photogrammetric Week '13*, 309-317. Stuttgart, Germany.

FGDC. (1998). *Geospatial Positioning Accuracy Standards. Part 3: National Standard for Spatial Data Accuracy*. Washington, DC: Federal Geographic Data Committee.

Filin, S. and Pfeifer, N. (2006). Segmentation of airborne laser scanning data using a slope adaptive neighbourhood. *ISPRS Journal of Photogrammetry and Remote Sensing*, 60: 71-80.

Gallant, J. C. (2000). *Terrain Analysis: Principles and Applications*. Hoboken, NJ: John Wiley & Sons.

Glennie, C. (2007). Rigorous 3D error analysis of kinematic scanning LiDAR systems, *Journal of Applied Geodesy*, 1: 147–157.

Greenwalt, C.R. and Shultz, M.E. (1962). *Principles of Error Theory and Cartographic Applications (No. ACIC-TR-96)*. St Louis, MO: Aeronautical Chart and Information Center.

Guan, H. (2013). *Automated Extraction of Road Information from Mobile Laser Scanning Data*, Doctoral Dissertation, University of Waterloo.

Guan, H., Li, J., Yu, Y., and Wang, C. (2013). Geometric validation of a mobile laser scanning system for urban applications, *MMT 2013*, Taiwan, China, 1-3 May 2013.

Guan, H., Li, J., Yu, Y., Chapman, M., and Wang, C. (2015a). Automated road information extraction from mobile laser scanning data. *IEEE Transactions on Intelligent Transportation Systems*, *16*(1): 194-205.

Guan, H., Li, J., Yu, Y., Chapman, M., Wang, H., Wang, C., and Zhai, R. (2015b). Iterative tensor voting for pavement crack extraction using mobile laser scanning data. *IEEE Transactions on Geoscience and Remote Sensing*, *53*(3): 1527-1537.

Gupta, K. (2007). Urban flood resilience planning and management and lessons for the future: a case study of Mumbai, India. *Urban Water Journal*, *4*(3): 183-194.

Heritage, G. and Large, A. (Eds.). (2009). *Laser Scanning for the Environmental Sciences*. Hoboken, NJ : John Wiley & Sons.

Hoppe, H., DeRose, T., Duchamp, T., McDonald, J., and Stuetzle, W. (1992), Surface Reconstruction from Unorganized Points, *ACM SIGGRAPH 1992 Conference Proceedings*, Chicago, USA, 71-78.

Johnston, K., Ver Hoef, J. M., Krivoruchko, K., and Lucas, N. (2001). *Using ArcGIS Geostatistical Analyst* (Vol. 380). Redlands, CA: ESRI.

Jwa, Y., and Sohn, G. (2012). A piecewise catenary curve model growing for 3d power-line reconstruction. *Photogrammetric Engineering and Remote Sensing, 78*(12): 1227-1240.

Kasser, M., and Egels, Y. (2002). *Digital Photogrammetry*. London: Taylor & Francis, 159-167.

Kayadibi, O. (2009). Recent advances in satellite technologies using to generate the digital elevation model (DEM). *Proceedings on IEEE 4th Recent Advances in Space Technologies*, New York, USA, 380–385

Kenward, T., Lettenmaier, D. P., Wood, E. F., and Fielding, E. (2000). Effects of digital elevation model accuracy on hydrologic predictions. *Remote Sensing of Environment*, *74*(3): 432-444.

Kilian, J., Haala, N. and Englich, N.(1996). Capture and evaluation of airborne laser scanner data. *ISPRS Archive*, *31*(B3): 383-388.

Kobler, A., Pfeifer, N., Ogrinc, P., Todorovski, L., Ostir, K. and Dzeroski, S. (2007). Repetitive interpolation: A robust algorithm for DTM generation from aerial laser scanner data in forested terrain. *Remote Sensing of Environment, 108*: 9-23.

Kukko, A., Jaakkola, A., Lehtomaki, M., Kaartinen, H., and Chen, Y. (2009). Mobile mapping system and computing methods for modelling of road environment. In *2009 Joint IEEE Urban Remote Sensing Event,* Shanghai, China. 1- 6.

Kukko, A., Kaartinen, H., Hyyppä, J., Chen, Y., (2012). Multiplatform mobile laser scanning: Usability and performance. *Sensors*, 12: 11712–11733.

Laslett, G.M., McBratney, A.B., Pahl, P.J., Hutchinson, M.F. (1987). Comparison of several spatial prediction methods for soil pH. *Journal of Soil Science,* 38: 325-341.

Lato, M., Hutchinson, J., Diederichs, M., Ball, D., and Harrap, R. (2009). Engineering monitoring of rockfall hazards along transportation corridors: using mobile terrestrial LiDAR, *Natural Hazards and Earth System Sciences*, 9: 935–946.

Leberl, F. (1973). Interpolation in square grid DTM, *The ITC Journal*. 756–807.

Ledoux, H., and Gold, C. (2005). An efficient natural neighbour interpolation algorithm for geoscientific modelling. In Fisher, P. (eds.), *Developments in Spatial Data Handling*. Springer, 97-108.

Li, J., and Heap, A. D. (2014). Spatial interpolation methods applied in the environmental sciences: A review. *Environmental Modeling and Software*, 53: 173-189.

Lichti, D.D. (2010). Terrestrial laser scanner self-calibration: correlation sources and their mitigation, *ISPRS Journal of Photogrammetric and Remote Sensing*, 65: 93–102.

Norrman, J., Eriksson, M., and Lindqvist, S. (2000). Relationships between road slipperiness, traffic accident risk and winter road maintenance activity. *Climate Research*, *15*(3), 185-193.

Lin, Y., and Hyyppa, J. (2010). Geometry and intensity based culvert detection in mobile laser scanning point clouds. *Journal of Applied Remote Sensing*, 41: 043553-043553.

Linh, T. H., and Laefer, D. F. (2014). Octree-based, automatic building facade generation from LiDAR data. *Computer-Aided Design*, 53: 46–61.

Liu, X. Y. (2008). Airborne LiDAR for DEM generation: some critical issues, *Progress in Physical Geography, 32*(1): 31-49.

Liu, Y., Du, M., Jing, C., and Cai, G. (2014). Design and implementation of monitoring and early warning system for urban roads waterlogging. In Li, D. and Chen, Y. (eds.), *Computer and Computing Technologies in Agriculture 8*, Springer, 610-615.

Maune, D. (2007). *Digital Elevation Model Technologies and Applications: The DEM Users Manual*, 2nd ed. Bethesda, MD: ASPRS Publications.

Meng, X.; Wang, L.; Currit, N. (2009). Morphology-based building detection from airborne

LIDAR data. *Photogrammetric Engineering and Remote Sensing*, 75: 427-442.

Mikhail, E. M. and Gracie, G. (1981). *Analysis and Adjustment of Survey Measurements*. NYC: Van Nostrand Reinhold. 340.

Moreira, J., (1996). Design of airborne interferometric SAR for high precision DEM generation, *ISPRS Archives*, *31*(B2): 256-260.

Natural Resources Canada. (2015). *Height Reference System Modernization.* Retrieved from http://www.nrcan.gc.ca/earth-sciences/geomatics/geodetic-reference-systems/9054.

Nurunnabi, A., West, G., and Belton, D. (2013). Robust locally weighted regression for ground surface extraction in mobile laser scanning 3D data, *ISPRS Annual, II-5*/W2, 217-222.

Olsen, M. J., Roe, G. V., Glennie, C., Persi, F., Reedy, M., Hurwitz, D., Williams, K., Tuss, H., Squellati, A., and Knodler, M. (2013). *Guidelines for the Use of Mobile LIDAR in Transportation Applications*. Washington, DC: NCHRP.

Optech, (2009). *ALTM Gemini*, http://www.optech.ca/pdf/Brochures/ALTM-GEMINI.pdf.

Petrie, G., and Toth, C. K. (2008). Introduction to laser ranging, profiling, and scanning. *Topographic Laser Ranging and Scanning: Principles and Processing*, 1-28.

Pfeifer, N. and Briese, C. (2007). Geometrical aspects of airborne laser scanning and terrestrial laser scanning, *ISPRS Archives*, *36* (3/W52): 311-319.

Pfeifer, N., and Boehm, J. (2008). Early stage of Lidar data processing, In Li, Z., Chen and Baltsavis, E. (eds.), *Advances in Photogrammetry, Remote Sensing and Spatial Information Sciences: 2008 ISPRS Congress Book*, London: Taylor and Francis, 169-

184.

Pfeifer, N., and Mandlburger, G. (2008). Lidar data filtering and DTM generation, In Shan, J. and Toth, C. K. (eds.). *Topographic Laser Scanning and Imaging: Principles and Processing*, CSC Press, 308-333.

Puente, I., González-Jorge, H., Martínez-Sánchez, J., and Arias, P. (2013). Review of mobile mapping and surveying technologies, *Measurement*, *46*(7): 2127-2145.

Rabbani, T., van den Heuvel, G., and Vosselman, G. (2006), Segmentation of point clouds using smoothness constraint, *ISPRS Avhieves*, *36*(5): 248-253.

Riaño, D., Valladares, F., Condés, S., and Chuvieco, E. (2004). Estimation of leaf area index and covered ground from airborne laser scanner (Lidar) in two contrasting forests. *Agricultural and Forest Meteorology*, *124*(3-4): 269-275.

Shan, J., and Toth, C. K. (2008). *Topographic Laser Ranging and Scanning: Principles and Processing*. Boca Raton, FL: CRC Press.

Sibson, R. (1981). A brief description of natural neighbour interpolation, In Barnet, V. (Eds.). *Interpolating Multivariate Data* (21–36), NYC: John Wiley & Sons.

Sithole, G., and Vosselman G. (2003). Comparison of filtering algorithms, *ISPRS Achieves, 34*(3-W13): 8.

Smadja, L., Ninot, J., and Gavrilovic, T. (2010). Road extraction and environment interpretation from LiDAR sensors. *ISPRS Archives*, *38*(3/A): 281–286.

Sohn, G., and Dowman, I. J. (2002). Terrain surface reconstruction by the use of tetrahedron model with the MDL criterion. *ISPRS Archives*, *34*(3/A): 336-344.

Takashi, O. and Kiyokazu, T. (2006). Lane recognition using on-vehicle LiDAR, *IEEE*

Intelligent Vehicles Symposium, Tokyo, Japan, 540-545.

Toutin, T. (2002). Three-dimensional topographic mapping with ASTER stereo data in rugged topography. *IEEE Transactions on Geoscience and Remote Sensing, 40*(10): 2241-2247.

Tovari, D. and Pfeifer, N. (2005). Segmentation based robust interpolation- a new approach to data filtering, *ISPRS Achieves, 36*(3-W19):79-84.

Vaaja, M., Hyyppä, J., Kukko, A., Kaartinen, H., Hyyppä, H., and Alho, P. (2011). Mapping topography changes and elevation accuracies using a mobile laser scanner. *Remote Sensing, 3*(3): 587–600.

Vanco, M. and Brunnett, G. (2007), Geometric preprocessing of noisy point sets: an experimental study, *Computing*, 79: 365-380.

Vaze, J., and Teng, J. (2007). High resolution LiDAR DEM–how good is it. In Oxley, L. and Kulasiri, D. (eds.). *2007 International Congress on Modelling and Simulation. Modelling and Simulation Society of Australia and New Zealand*, 692-698.

Veneziano, D., Hallmark, S., and Souleyrette, R. R. (2002). *Comparison of LIDAR & Conventional Mapping Methods for Highway Corridor Studies*. Ames, IA: Center of Transportation Research and Education, Iowa State University.

Vosselman, G. (2000). Slope based filtering of laser altimetry data. *ISPRS Archives*, *33*(B3/2): 935-942.

Vosselman, G. and Maas, H. (2001). Adjustment and filtering of raw laser altimetry data, *Proceedings of OEEPE Workshop on Airborne Laser Scanning and Interferometric SAR for Detailed Digital Elevation Models*, 1-3 March, Stockholm, Sweden, 1(3).

Wack, R. and Wimmer, A. (2002). Digital terrain models from airborne laser scanner data - A grid based approach. *ISPRS Archives, 34*(3B): 293-296.

Walsh, S. B., & Hajjar, J. F. (2009). *Data Processing of Laser Scans Towards Applications in Structural Engineering*. Champaign, IL: Newmark Structural Engineering Laboratory, University of Illinois at Urbana-Champaign.

Wang, C., Menenti, M., Stoll, M. P., Alessandra, F., Enrica, B., and Marco, M. (2009). Separation of ground and low vegetation signatures in lidar measurements of salt-marsh environments. *IEEE Transactions on Geoscience and Remote Sensing*. 47: 2014-2023.

Watson, D. (1992). *Contouring: A Guide to the Analysis and Display of Spatial Data*. London: Pergamon Press.

Webster, R., and Oliver, M. (2001). *Geostatistics for Environmental Scientists*. Chichester, UK: John Wiley & Sons.

Weibel, R., and Heller, M. (1993). *Digital Terrain Modelling*. Oxford, UK: Oxford University Press.

Wen, C., Li, J., Luo, H., Yu, Y., Cai, Z., Wang, H., and Wang, C. (2015). Spatial-related traffic sign inspection for inventory purposes using mobile laser scanning data. *IEEE Transactions on Intelligent Transportation Systems*, *17*(1): 27-37.

Williams, K., Michael, J.O., Gene, V.R., and Glennie, C. (2013). Synthesis of transportation applications of mobile LiDAR. *Remote Sensing*, 5: 4652-4692.

Wilson, J. P., and Gallant, J. C. (2000). *Terrain Analysis: Principles and Applications*. Hoboken, NJ: John Wiley & Sons.

Xu, H., Cheng, L., Li, M., Chen, Y., and Zhong, L. (2015). Using octrees to detect changes to buildings and trees in the urban environment from airborne Lidar data. *Remote Sensing*, 78: 9682-9704.

Yang, B., Fang, L., and Li, J. (2013). Semi-automated extraction and delineation of 3D roads of street scene from mobile laser scanning point clouds. *ISPRS Journal of Photogrammetry and Remote Sensing*, 79: 80-93.

Yen, K. S., Akin, K., Lofton, A., Ravani, B., and Lasky, T. A. (2010). *Using mobile laser scanning to produce digital terrain models of pavement surfaces*. Davis, CA: AHMCT Research Center.

Yen, K. S., Ravani, B., and Lasky, T. A. (2011). *Lidar for Data Efficiency* (WA-RD 778.1). Washington, DC: Washington State Department of Transportation.

Yu, Y., Guan, H., and Ji, Z. (2015a). Automated detection of urban road manhole covers using mobile laser scanning data. *IEEE Transactions on Intelligent Transportation Systems*, *16*(6): 3258-3269.

Yu, Y., Li, J., Guan, H., and Wang, C. (2015b). Automated extraction of urban road facilities using mobile laser scanning data. *IEEE Transactions on Intelligent Transportation Systems, 16*(4): 2167-2181.

Yuan, X., Zhao, C., and Zhang, H. (2010). Road detection and corner extraction using high definition LiDAR, *Information Technology Journal*, 9: 1022-1030.

Zhang, K. Q., Chen, S. C., Whitman, D., Shyu, M. L., Yan, J. H. and Zhang, C. C. (2003). A progressive morphological filter for removing nonground measurements from airborne lidar data, *IEEE Transactions on Geoscience and Remote Sensing,* 41: 872–

882.

Zippelt, K. and Czerny, R. (2010). Collection and interpretation of point clouds of terrestrial laser scanning as a basis for hydraulic flow modelling. *FIG Congress,* Sydney, Australia. Retrieved from: https://www.fig.net/resources/proceedings/fig_proceedings/fig2010/papers/ts03d/ts03d_zippelt_czerny_4374.pdf

Zomer, R., Ustin, S., and Ives, J. (2002). Using satellite remote sensing for DEM extraction in complex mountainous terrain: landscape analysis of the Makalu Barun National Park of eastern Nepal. *International Journal of Remote Sensing, 23*(1): 125-143.